

# An extension of a model of texture induced anisotropy in polycrystalline materials

Brandon C. Templin

Center for Advanced Vehicular Systems  
Mississippi State University, Mississippi State, MS 39762

Adetokunbo A. Adedoyin

Los Alamos National Laboratory, P.O. Box 1663, Los Alamos, NM 87545  
Email: aadedoyin@lanl.gov

Koffi Enakoutsa

Department of Mathematics, UCLA  
520 Portola Plaza, Los Angeles, CA 90095

Douglas J. Bammann

Center for Advanced Vehicular Systems  
Mississippi State University, Mississippi State, Mississippi 39762

---

## Abstract

A dislocation based internal state variable model of plasticity is modified to capture evolving anisotropy resulting from underlying texture. Anisotropy is modeled via a second order orientation tensor resulting from the truncation to second order of an orientation distribution function and the temporal evolution of the tensor arises naturally from the closure properties associated with the truncation. A scalar variable defined by the Euclidean norm of the current state of the structure tensor and the direction of the rate of continuing plastic deformation, is incorporated first in the flow rule and then in the evolution of the state variables. The model is compared with yield surface data after various preloads for Aluminum 1100-O, differences in compression versus torsion for 304L SS and large directional changes in load path for AL 1100-O. Finally, comparison is made between the different forms of the anisotropy in the prediction of the yield surfaces. Additional assessments of the model which compared the predictions of the model with and without textural effects are provided.

*Keywords:* Texture, Anisotropy, Structure Tensor, Orientation Distribution Function



## 1. Introduction

Various modeling techniques are employed to predict the effects of texture and anisotropy. Some of the most prevalent methods found throughout the literature include crystal plasticity models, anisotropic yield functions, or through the incorporation of a coaxiality factor, a scalar variable describing the orientation of deformation with respect to some directionally dependent variables.

Crystal plasticity models are often used for prediction and modeling of texture. Rather than a continuous form for the plastic velocity gradient, crystal plasticity models introduce a discrete flow rule in which it is assumed that the plastic velocity gradient is the sum of plastic slip rate occurring on different slip systems of different orientations. The resolved shear stress on each slip system is the driving force for the plastic slip rate. Since each grain in a polycrystalline is aligned with a different orientation, grain to grain variations are modeled through a Taylor assumption (overall compatibility is assured by the assumption that each grain deforms with the same velocity gradient, but equilibrium between the grains is not satisfied), a Sachs assumption (equilibrium between the grains is satisfied with loss of compatibility) or self consistency models that approximately satisfy both compatibility and equilibrium between grains. An extensive description on the development and application of crystal plasticity models is found in Dawson et al. [1]. Extending from the work by Pierce et al. [2], Becker is often described as the first to incorporate the 12 FCC slip systems into a polycrystalline simulation using a crystal plasticity model[3, 4]. However, Mathur and Dawson [5] extended the work presented by Kocks [6, 7] to implement a material point simulator capable of predicting the evolving texture of Aluminum 1100 following various deformation modes using a power law hardening and a Voce type slip system hardening law. A multitude of simulations employing crystal plasticity models have been implemented, for an exhaustive list of models incorporating crystal plasticity the reader is referred to Roters et al. [8]. With the implementation of a crystal plasticity model, a material point is often divided into a discrete number of grains termed the representative volume element. By employing numerical techniques, such as enforcing compatibility,

self-consistency, or equilibrium of the individual grains, the orientation and rotation of each grain is calculated and updated at various deformation increments. Van Houtte et al. [9] found that the degree of accuracy in texture and anisotropic behavior in crystal plasticity predictions is directly linked to the number of discrete grains contained within each representative volume element. Two numerical aspects must be considered when implementing a crystal plasticity model, the size of the Jacobian matrix and the character of the equations being implemented. Due to large variations in strain with small variations in stress, the shear rate on each slip system is often chosen as model inputs. The Jacobian matrix can become quite large due to each grain possessing up to 12 slip systems for FCC materials or up to 48 slip systems for BCC materials. The large Jacobian matrix results in the model being computationally expensive and will require a lot of processor time to run a large body simulation. Aside from using RVE, a material point can be described as a single or portion of a single grain in a crystal plasticity model. Due to the small volume of a single grain when compared to the volume of a typical component, defining a material point as single grain is not feasible for large scale simulations.

Some of the earliest models to consider polycrystalline materials were proposed by Taylor [10, 11, 12], Sachs and Bishop-Hill [13, 14]. The most widely used and generally accepted anisotropic model is that proposed by Hill which is a modification of the Von Mises yield criterion to incorporate anisotropy through the inclusion of several scalar parameters. The quadratic Hill yield criterion is defined

$$1 = F(\sigma_{22} - \sigma_{33})^2 + G(\sigma_{33} - \sigma_{11})^2 + H(\sigma_{11} - \sigma_{22})^2 + 2L\sigma_{23}^2 + 2M\sigma_{31}^2 + 2N\sigma_{12}^2 \quad (1)$$

where  $\sigma_{ij}$  are components of the stress tensor and F,G,H,L,M,N are scalar constants describing anisotropic behavior. A generalized yield criterion was proposed by Hershey [15] that captures both Von Mises and Tresca yield conditions depending on the choice of a single material parameter. A commonly used set of anisotropic yield functions are based from a linear transformation of the deviatoric stress tensor in a Hershey

type yield criterion [16]:

$$4\bar{\sigma}^a = \sum_{i,j}^{1,3} |\tilde{S}'_i - \tilde{S}''_j|^a \quad (2)$$

where  $\tilde{S}'$  and  $\tilde{S}''$  are transformed stress deviators transformed via non symmetric fourth order anisotropy tensors  $C'$  and  $C''$  respectively and  $a$  is a constant coefficient. Some of the more commonly used yield criterion of this type include the yld2004-18p [17], the yld91 [16], and the yld2000-2d [18]. The main differences separating the different yield models is the number of parameters required to capture anisotropy with an obvious improvement in predictive capability with increased parameters. For example, the yld2004-18p has 18 parameters, yld91 is a particular case of the yld2004-18p model with 6 anisotropic parameters, and yld2000-2d has 10 anisotropic parameters. The number of parameters required to describe anisotropy in each of these models is dependent on assumptions made about the fourth order transformation tensors and whether the two transformation tensors are equivalent. Each anisotropic parameter is determined via individual testing which may include but is not limited to uniaxial extension, balanced biaxial flow tests, bulge tests, and disc compression tests. The material parameters in these models describe anisotropy by considering the directionality of the flow stresses (y-values) and/or the thickness to width strain ratios (r-values) and are generally determined based on the initial anisotropy of the material. Yoon et al. [19] considered the influence of the r-values and y-values separately on the earing profile in a cup drawing process. Taherizadeh et al. [20] compared three anisotropic models, Hill, non associative yld91, and yld2000 in various sheet metal forming processes. They found each model to have different degrees of accuracy in different loading conditions and determined the springback simulations to be more dependent of the hardening model than the anisotropic yield criterion. Kuwabara et al. [21] also compared various yield criterion, Von Mises, Hill, yld2000 in and anisotropic hole punch test. They determined that the anisotropic yield conditions were more accurate, with the yld2000 offering the highest degree of accuracy.

Anisotropic simulations described by the initial anisotropy of the material may be sufficient for single pass forming simulations, but these models preserve the initial

anisotropy of the material. It has been experimentally demonstrated that a change in the direction of deformation will have a significant contribution on the materials current texture which in turn impacts the materials yield response. Phillips [22, 23, 24], Stout et al. [25] and Brown [26] experimentally observed significant changes in the orientation and shape of the yield surface by probing the yield surface at various prestrains and using a five microstrain offset definition of yield. Both Stout and Brown observe a change in the shape and orientation of the yield surface. In addition to isotropic and kinematic hardening to describe the evolution of an anisotropic yield surface, the change in shape and rotation of the yield surface are described by distortional and rotational hardening respectively. It is important to understand that the observed anisotropy of initial yield is strongly dependent upon the definition of yield. Stout demonstrated that for a large definition of yield (say, a .02% offset), the initial yield surface is nearly isotropic, however the anisotropy increases with strain. Wegener and Schlegel [27] characterize this anisotropic behavior as a flattening, sharpening, symmetric shrinking, and symmetric expansion of the yield surface with respect to the direction of plastic deformation. Hahn and Kim [28] observed a rotation of the material orthotropic axes by calculating anisotropic parameters of uniaxial tests at various angles to the rolling direction of 3 and 6 percent prestrained aluminum sheet. Khan et al. [29] investigate asymmetrical yield surfaces for larger strain offset definitions from tension/torsion experiments. Armstrong and Hockett [30] observed an apparent softening in large strain compression testing of Aluminum cubes under large load path changes. Miller recorded a difference in hardening behavior in compression and torsion as well as compression to torsion and torsion to compression load path changes [31]. Kubawara et al. [32] noted differential hardening in 2 of 6 uniaxial specimens in uniaxial tests taken at various angles to the orthotropic axes of steel sheet with known initial texture. Anisotropic strain hardening was observed in uniaxial and shear testing of Al sheet in Lopes et al. [33]. They also observed a difference in orientational hardening behavior between uniaxial tension and shear in which uniaxial tension specimens exhibited more hardening and maximum strain at 45 degrees to the rolling direction, while shear specimens exhibited more initial hardening at 90 degree orientation with a longer hardening transient at a 45 degree orientation.

Adebarro et al. [34, 35, 36] incorporated temperature dependence to the anisotropic terms of the yld96 yield surface. They calculated the anisotropic terms at several different temperatures and then used 3<sup>rd</sup> and 5<sup>th</sup> order polynomials to fit the parameters and include them into their simulation. Aretz [37] incorporated strain dependent anisotropic terms using the yld2003 model by calculating the anisotropic terms at four finite strains. The strain dependence of the anisotropic terms was then incorporated into a simulation via a look-up table and linear interpolation. Stoughton and Woon [38] proposed a model to incorporate scalar distortional hardening by replacing the initial directional flow stress terms used to determine the anisotropic parameters with four separate stress-strain relations. They also noted a significant reduction in the systematic error in calculations in all loading directions using a model that includes distortional hardening, they suggest including distortional hardening may be required for advanced material models with non proportional loading. A very large number of yield surfaces have been proposed based upon modifications of these approaches (higher order Hill, stress invariants, linear transformation, crystal plasticity, etc.). For example, Li et al (2016) proposed an anisotropic yield surface using a combination of stress invariant and shear stress [39], Yoon et al. (2014) proposed an asymmetric yield surface based upon stress invariants [40], Lee et al. (2017) proposed a higher order yield surface [41]. Other proposed yield surface definitions can be found such as, Lester and Scherzinger (2018) [42], Lee et al. (2018) [43], Lou and Yoon (2018) [44], Kabirian and Khan (2015) [45], Cardoso and Adetoro (2017) [46], Kim et al. (2017) predicted evolving anisotropy with an advanced crystal plasticity model [47] and Zhang et al (2015) utilized a Self Consistent Viscoplasticity approach [48].

Anisotropy has also been accounted for through the inclusion of a scalar coaxiality parameter describing the angle between the direction of plastic flow and some directionally dependent variable, a concept first introduced by Key and Krieg [49]. One common form of the coaxiality term follows that suggested by Schmitt et al. [50]:

$$\theta = \frac{\epsilon_p}{\|\epsilon_p\|} : \frac{\epsilon}{\|\epsilon\|} \quad (3)$$

where  $\epsilon_p$  is the strain tensor associated with the prestrain and  $\epsilon$  is the strain tensor associated with the subsequent strain. This form of the coaxiality term is motivated from the dissolution of substructure formed during the prestrain step which corresponds with the findings by Schmidt et al. [50] that new substructure formation is only correlated with the subsequent strain. Teodosiu and Hu [51, 52] suggest a substructure motivated anisotropic model using a similar form of the coaxiality term and a parameter  $\beta_s$  that is similar to the parameter  $\theta$ . The  $\beta_s$  presented by Teodosiu and Hu introduces anisotropy into their four internal state variable model as the scalar product of a prestrain rate tensor and a subsequent strainrate tensor. Further applications and extensions of this model include [53, 54, 55, 56, 57, 58, 59]. Employing a coaxiality term following this formulation introduces an inherent difficulty in tracking rapidly changing loading directions. Models employing this form of coaxiality term generally have the backstress evolve with the applied stress versus the plastic deformation.

Evolving anisotropy has been modeled using a scalar coaxiality term that describes the coaxiality between the kinematic hardening and direction of plastic flow:

$$\cos \theta = \frac{\boldsymbol{\alpha}}{\|\boldsymbol{\alpha}\|} : \frac{\mathbf{d}_p}{\|\mathbf{d}_p\|} \quad (4)$$

where  $\boldsymbol{\alpha}$  is an internal state variable associated with the backstress due to GNDs and  $\mathbf{d}_p$  is the direction of plastic flow. Bammann and Aifantis [60] derived an expression for the plastic spin from single slip and in conjunction with this coaxiality factor matched experimental observations of both free and fixed end axial effects in the torsion of circular cylinders. They also demonstrated that this modeling approach could accurately match crystal plasticity calculations in large strain shear [61]. Miller et al. [62] introduced a kinematic hardening evolution equation with an exponential dependence on a similar coaxiality term in an effort to replicate the rapid evolution of the flow stress in sudden load path changes of Oxygen Free High Conductivity (OFHC) Copper specimens with various amounts of rolling reduction. A parameter of this type was first introduced in the hardening of a tensorial variable by Key and Krieg [49] in an effort to capture the shape of the uniaxial tensile stress in a load reversal. Wegener and Scheelge [27] suggested a kinematic hardening evolution equation dependent on

a coaxiality term to maximize the effect of hardening for a given change of plastic strain. Francois [63] described a distorted yield surface as a “hyper egg” and suggested a model that can capture a hyper egg type yield surface through the inclusion of a parameter following the angle between the distorted stress and backstress allowing for a description of all possible states with a reduced set of variables. Shutov and Ihlemann [64] proposed a model with improved control of distortional hardening through the inclusion of a backstress-like second order distortional stress in which the yield criterion is dependent on the angle between the effective stress and the distortional stress. Bammann et al. [65] introduced the dependence of the isotropic hardening on a similar coaxiality term in order to account for the reduction in saturation stress of a specimen experiencing cyclic loading. Chaboche [66] discussed a similar coupling of isotropic and kinematic hardening to account for cyclic hardening and softening.

Recent inclusions of a coaxiality type term of the form proposed by Barlat et al. [67]

$$\cos \theta = \frac{8}{3} \hat{\mathbf{s}} : \hat{\mathbf{h}} \quad (5)$$

where  $\hat{\mathbf{h}}$  is a normalized structural tensor referred to as the microstructure history deviator and  $\hat{\mathbf{s}}$  is the normalized stress deviator. This form is based on the assumption that the deviatoric stress and the plastic strain rate tensor have the same direction. Further applications of this model load path changes of mild steel [68], cross load and reverse load of high strength and mild steel [69], and low carbon steels under double load path changes [70].

A strong motivation for this work is the coaxiality term presented in Regeuro et al. [71]

$$\cos \theta = \frac{\mathbf{a}}{\|\mathbf{a}\|} : \frac{\mathbf{d}}{\|\mathbf{d}\|} \quad (6)$$

where  $\mathbf{d}$  is the plastic stretch tensor.  $\mathbf{a}$  is a second order orientation tensor defined by Prantil [72, 73] that describes the orientation distribution function of a unit vector bisecting the active slip systems in double planar slip. This orientation tensor evolves similar to the backstress and provides a mean to represent texture in a manner that

evolves independent of the kinematic hardening. The orientation tensor stems from the tensorial expansion of the orientation distribution function by Onat and Leckie [74] and follows the basic form presented in Advani and Tucker [75, 76]. Orientation tensors of this kind have been used to represent various anisotropic behaviors in materials [77, 74, 78, 79, 80, 81, 82].

Aside from anisotropic yield functions, coaxiality terms, or crystal plasticity, anisotropy is also modeled using an orientation distribution function (ODF) or tensorial variable describing the distribution function. Rashid [83] determined the orientational effects of yield stress of a polycrystalline material in biaxial extension and simple shear by determining exact solutions of the ODF for the respective boundary conditions, then applying the ODF to the flow stress through orientation averaging. Ning and Aifantis [84] proposed an anisotropic model that incorporates anisotropy through a fourth order orientation tensor calculated from the ODF that is applied to the flow rule, flow stress, and kinematic hardening. Cho and Dafalias [85] introduce a model that incorporates anisotropy through a constitutive spin and selection of material parameters.

In this work, evolving anisotropy is modeled via a modified version of the Evolving Microstructural Model of Inelasticity (EMMI) presented by Marin et al. [86]. Material anisotropy is characterized by a second order orientation tensor and included in the flow rule via a scalar variable describing the coaxiality of the second order orientation tensor and the direction of plastic deformation. The motivation is to develop high-fidelity computational design tools for metallic structures. The representation of material anisotropy using a second order orientation tensor allows for the evolution of anisotropy independent of the kinematic hardening. The model is then tested against anisotropic yield data of Aluminum 1100-O presented by Brown [26]. The rest of the paper is structured as follows.

- The first section describes the original EMMI model constitutive equations and its extended version to account for anisotropic and texture effects using structure tensor as described above.

- The following section compares the analytical yield surface the modified EMMI model predicts with the experimental results of Brown [26] for several sets of the model parameters and different strategies to include anisotropic and texture effects in the EMMI model. Besides these comparisons, the section presents the texture effects predictive capacities of the model for simple and complex loads.
- Finally, the third section presents an additional assessment of the model. The response of the material for the cases where the model accounts for textural effects or not were demonstrated for complex loading conditions.

The following mathematical operations in direct notation are used in the remainder of this paper. All Bold face Greek or alphabetical letters indicate a tensorial quantity. Therefore given the following second rank tensorial quantities  $\mathbf{A}$ ,  $\mathbf{B}$ ,  $\mathbf{C}$  and scalar variable  $\gamma$ , the norm of tensorial quantity is equivalent to  $\|\mathbf{A}\| = [\mathbf{A} : \mathbf{A}]^{\frac{1}{2}}$  where the colon indicates a double contraction. The trace of a tensorial quantity is equivalent to  $\text{Tr}[\mathbf{A}] = \mathbf{A} : \mathbf{I}$ . The deviatoric portion of a tensorial quantity is equivalent to  $\hat{\mathbf{A}} = \mathbf{A} - \frac{1}{3}\text{Tr}[\mathbf{A}]\mathbf{I}$ . The product of two second rank tensorial quantities is equivalent  $\mathbf{AB} = \mathbf{C}$ . Associativity and Distributivity with respect to  $\gamma$  in conjunction with the tensorial quantities  $\mathbf{A}$ ,  $\mathbf{B}$  and  $\mathbf{C}$  hold for cases where scalar or vector sums are valid mathematical operations.

## 2. Methodology

### 2.1. The Constitutive equations of the anisotropic EMMI model

The model used in this study is the Evolving Micro-structural Model of Inelasticity (EMMI) outlined in Marin et al. [86] modified to accommodate material anisotropy. The EMMI model is a temperature and rate dependent phenomenological model that uses two internal state variables to capture material hardening. The constitutive equations of the EMMI model consist of the following elements.

#### 2.1.1. Kinematics

The EMMI model equations are derived in the intermediate configuration stemming from the multiplicative split of the deformation gradient as presented by Lee and

Liu [87] and Lee [88]. The deformation gradient is given by:

$$\mathbf{F} = \mathbf{F}_e \mathbf{F}_p \quad (7)$$

where  $\mathbf{F}_p$  is the plastic part of the total deformation gradient that facilitates mapping relevant variables from the reference material configuration to the intermediate. Similarly,  $\mathbf{F}_e$  is the elastic part of the total deformation gradient that aids in mapping relevant variables from the intermediate configuration to the current. The intermediate configuration is a load free configuration associated with permanent deformation due to internal defects while the current configuration represents a material configuration with an applied load. Following the thermodynamics for materials with internal state variables presented by Coleman and Noll [89] and Coleman and Gurtin [90], the model equations are derived in a compatible load free intermediate configuration and then pushed forward to the current configuration. The velocity gradient determined using Eq.(7) is:

$$\mathbf{l} = \dot{\mathbf{F}} \mathbf{F}^{-1}. \quad (8)$$

Therefore, the symmetric and an antisymmetric portions of the velocity gradient are:

$$\mathbf{d} = \frac{1}{2} [\mathbf{l} + \mathbf{l}^T], \quad \mathbf{w} = \frac{1}{2} [\mathbf{l} - \mathbf{l}^T]. \quad (9)$$

Both portions of the velocity gradient can further be decomposed into an elastic and plastic parts such that:

$$\mathbf{d} = \mathbf{d}_e + \mathbf{d}_p, \quad \mathbf{w} = \mathbf{w}_e + \mathbf{w}_p. \quad (10)$$

### 2.1.2. Evolution equations for the internal state variables

Assuming linear elasticity and a homogeneous isotropic material the Cauchy stress rate is:

$$\dot{\boldsymbol{\sigma}} = \dot{\boldsymbol{\sigma}} - \mathbf{w}_e \boldsymbol{\sigma} + \boldsymbol{\sigma} \mathbf{w}_e = \frac{\boldsymbol{\sigma}}{\mu(\theta)} \frac{\partial \mu(\theta)}{\partial \theta} \dot{\theta} + 2\mu(\theta) \dot{\mathbf{d}}_e + B(\theta) \text{Tr}(\mathbf{d}_e) \mathbf{I} \quad (11)$$

where  $\mu(\theta)$  is the temperature dependent shear modulus,  $B(\theta)$  is the temperature dependent bulk modulus, and  $\dot{\mathbf{d}}_e$  is the deviatoric part of the symmetric portion of the velocity gradient determined by:

$$\dot{\mathbf{d}}_e = \dot{\mathbf{d}} - \mathbf{d}_p. \quad (12)$$

### 2.1.3. Isotropic hardening

The isotropic hardening internal state variable is associated with the annihilation and generation of statistically stored dislocations (SSD) where its evolution equation is cast in a hardening minus recovery format. The dynamic recovery portion was introduced by Kocks and Mecking [91] and Esterin and Mecking [92], while the static recovery portion was presented by Nes [93]. The evolution equation is given by:

$$\dot{\kappa} = \frac{\kappa}{\mu(\theta)} \frac{\partial \mu(\theta)}{\partial \theta} \dot{\theta} + (H_\kappa - R_d \kappa) \dot{\epsilon}_p - R_s \kappa \sinh\left(\frac{Q_s}{2\mu C_\kappa} \kappa\right) \quad (13)$$

where  $R_d(\theta)$  is the dynamic recovery parameter,  $R_s(\theta)$  is the static recovery parameter, and  $Q_s$  determines the order of the static recovery. The isotropic hardening modulus ( $H_\kappa$ ) is reduced to a single variable given by:

$$H_\kappa = 2\mu(\theta) C_\kappa H \quad (14)$$

### 2.1.4. Kinematic hardening

The back-stress is a stress-like internal state variable associated with the annihilation and generation of geometrically necessary dislocation (GND). In a similar approach, the evolution equation for the back-stress is cast in a hardening minus recovery format given by the equation

$$\dot{\alpha} = \dot{\alpha} - \mathbf{w}_e \alpha + \alpha \mathbf{w}_e = \frac{\alpha}{\mu(\theta)} \frac{\partial \mu(\theta)}{\partial \theta} \dot{\theta} + h_\alpha \mathbf{d}_p - r_d \dot{\epsilon}^p \sqrt{\frac{2}{3}} \|\alpha\| \alpha \quad (15)$$

where  $r_d(\theta)$  is the recovery parameter and  $h_\alpha$  is the kinematic hardening modulus which is reduced to a single variable

$$h_\alpha = 2\mu(\theta) C_\alpha h \quad (16)$$

for simplicity.

### 2.1.5. Plastic flow

The plastic flow rule is given by:

$$\dot{\epsilon}_p = f(\theta) \sinh\left[\frac{\sigma_{eq}}{\kappa + Y_0} - 1\right]^{m(\theta)} \quad (17)$$

where  $\theta$  is the temperature variable,  $m(\theta)$  and  $f(\theta)$  are temperature dependent constants associated with the rate sensitivity of the material, and  $Y_0$  is the initial yield stress of the material.  $\kappa$  and  $\alpha$  are internal state variables associated with annihilation and generation of SSDs and GNDs, respectively. The equivalent stress is given by:

$$\sigma_{eq} = \sqrt{\frac{3}{2} \|\xi\|} \quad (18)$$

where  $\xi$  is:

$$\xi = \dot{\sigma} - \frac{2}{3}\alpha \quad (19)$$

and  $\dot{\sigma}$  is the deviatoric portion of the Cauchy stress.

## 2.2. Anisotropic flow rule

The evolution of anisotropy is represented by a second order orientation tensor outlined by Advani and Tucker [75, 76] and applied to polycrystalline materials by Prantil [72], in which the orientation tensor is defined by the ODF of a unit vector bisecting two active slip systems. The rate of change of material anisotropy is captured using the orientation tensor given by the equation:

$$\dot{\mathbf{a}} = \dot{\mathbf{a}} - \mathbf{w}_e \mathbf{a} + \mathbf{a} \mathbf{w}_e = \lambda_g \left( \mathbf{a} \mathbf{d}_p + \mathbf{d}_p \mathbf{a} + \frac{2}{3} \mathbf{d}_p \right) + \frac{2}{3} \lambda_g (\mathbf{a} : \mathbf{d}_p) \mathbf{I} - 2\lambda_g [\mathbf{B} : \mathbf{d}_p] \quad (20)$$

where  $\lambda_g$  is a fitted parameter associated with the orientation of active slip systems and  $\mathbf{B}$  is a fourth order orientation tensor defined as

$$B_{ijkl} = \oint F(\omega) \omega_i \omega_j \omega_k \omega_l d\omega \quad (21)$$

where  $F(\omega)$  is the orientation distribution function and  $\omega$  is the unit vector bisecting two active slip systems. Details on the derivation of Eq.(20) are not easily accessible and for this reason only a summary of the process yielding to this equation is given here. A short presentation of the derivation of these equations is also provided in (Appendix A). This presentation is not indispensable but useful for a full grasp of the foundations of the model.

A closure approximation is required in order to reduce the fourth order orientation tensor to a function of the second order orientation tensor while maintaining

all required symmetries of the higher order tensor. Linear and quadratic closure approximations are two commonly used closure approximations in which Advani and Tucker [75, 76] showed that the linear closure approximation is exact for completely random orientations and the quadratic closure approximation is exact for highly aligned orientations. In order to maintain a higher degree of accuracy through all orientations, they recommend a hybrid closure approximation that is a linear combination of the linear and quadratic closure approximations using a scalar measure of orientation. The contraction operation  $\mathbf{B} : \mathbf{d}_p$  is given by:

$$\mathbf{B} : \mathbf{d}_p = \frac{1}{7} [1 - f_a] [(\mathbf{a} : \mathbf{d}_p)\mathbf{I} + 2\mathbf{a}\mathbf{d}_p + 2\mathbf{d}_p\mathbf{a}] + \frac{2}{35} [f_a - 1] \mathbf{d}_p + f_a [\mathbf{a} : \mathbf{d}_p] \mathbf{a} \quad (22)$$

where  $f_a$  is a scalar measure of orientation given by:

$$f_a = \frac{3}{2} \mathbf{a} : \mathbf{a}^T - \frac{1}{2}. \quad (23)$$

The evolving anisotropy is incorporated into the flow rule of the EMMI model through a scalar coaxiality term used to describe the degree of alignment between the direction of plastic flow and anisotropy and is given by:

$$\eta(\bar{\eta}) = C_1 \cos(\bar{\eta}) + C_2 \cos(2\bar{\eta}) + C_3 \cos(3\bar{\eta}) + C_4 \cos(4\bar{\eta}). \quad (24)$$

where  $C_1, C_2, C_3$  and  $C_4$  are fitted anisotropic parameters. The variable  $\bar{\eta}$  is given by the equation:

$$\cos(\bar{\eta}) = \frac{\mathbf{a}}{\|\mathbf{a}\|} : \frac{\mathbf{d}_p}{\|\mathbf{d}_p\|} \quad (25)$$

where  $\mathbf{a}$  is the orientation tensor. The form of the coaxiality term is extended from the work presented by Lubrada and Krajcinovic [77] where they solved for the ODF equation by expanding the dot product of various damage orientation tensors with random direction tensors. This technique was later applied to polycrystalline materials by Rogeiro et al. [94]. Similar forms of  $\phi$  were presented in the works of Wegener and Schlegel [27], Bammann et al. [65], Miller et al. [62], and Francois [63] where  $\phi$  was defined using the direction of the back-stress and the plastic flow. The anisotropic

parameters must sum up to unity, that is:

$$\sum_{n=1}^4 C_i = 1; \quad (26)$$

this ensures that  $\eta = 1$  when the direction of plastic flow is coaxial with the direction of developed anisotropy.

The symmetric portion of the velocity gradient is given by:

$$\mathbf{d}_p = \sqrt{\frac{3}{2}} \dot{\bar{\epsilon}}_p \mathbf{N} \quad (27)$$

where  $\mathbf{N}$  is the modified direction of plastic flow. The scalar quantity  $\dot{\bar{\epsilon}}_p$  is the equivalent plastic strain rate modified to account for the anisotropic behavior [94] which is defined as:

$$\dot{\bar{\epsilon}}_p = f(\theta) \sinh \left[ \frac{\sigma_{eq}}{\eta(\bar{\eta}) \kappa + Y_0} - 1 \right]^{m(\theta)} \quad (28)$$

where  $m(\theta)$  and  $f(\theta)$  are constants associated with the rate sensitivity of the material.  $\eta(\bar{\eta})$  is the scalar coaxiality term and  $Y_0$  is the initial yield stress of the material. The variables  $\kappa$  and  $\alpha$  are internal state variables associated with annihilation and generation of SSDs and GNDs, respectively. The equivalent stress is given by:

$$\sigma_{eq} = \sqrt{\frac{3}{2}} \|\xi\| \quad (29)$$

where  $\xi$  is:

$$\xi = \dot{\sigma} - \frac{2}{3} \alpha \quad (30)$$

and  $\dot{\sigma}$  is the deviatoric portion of the Cauchy stress.

The modified direction of plastic flow must account for the directional effects of material anisotropy and is therefore given by:

$$\mathbf{N} = \frac{\mathbf{n}_T}{\|\mathbf{n}_T\|} \quad (31)$$

where  $\mathbf{n}_T$  is defined as:

$$\mathbf{n}_T = \mathbf{n}_\sigma - C_{\sigma\eta} \mathbf{n}_A \quad (32)$$

where  $\mathbf{n}_\sigma$  is the direction of the equivalent stress given by:

$$\mathbf{n}_\sigma = \frac{\boldsymbol{\xi}}{\|\boldsymbol{\xi}\|}. \quad (33)$$

The scalar  $C_{\sigma\eta}$  is the ratio:

$$C_{\sigma\eta} = \frac{\sigma_{eq}}{\eta(\bar{\eta})}. \quad (34)$$

Details on the derivation of Eqs.(31, 32, 33, 34) and the ensuing equations Eqs.(35, 36, 37, 38, 39) are provided in Appendix A and Appendix B.

The direction of plastic flow imposed by the anisotropic term  $\mathbf{n}_A$  is defined by:

$$\mathbf{n}_A = \zeta(\bar{\eta}) \left( \mathbf{a} - C_{\xi\mathbf{a}} \frac{\boldsymbol{\xi}}{\|\boldsymbol{\xi}\|} \right) \quad (35)$$

where the scalar  $\zeta(\bar{\eta})$  is given by the expression

$$\begin{aligned} \zeta(\bar{\eta}) = & m [C_1 + 4C_2 \cos(\bar{\eta}) + 3C_3 (4 \cos^2(\bar{\eta}) - 1)] \\ & + m [16C_4 \cos(\bar{\eta}) (2 \cos^2(\bar{\eta}) - 1)] \end{aligned} \quad (36)$$

where  $m$  is defined as

$$m = [\|\boldsymbol{\xi}\| \|\mathbf{a}\|]^{-1}. \quad (37)$$

The scalar  $C_{\xi\mathbf{a}}$  is given by:

$$C_{\xi\mathbf{a}} = \frac{\boldsymbol{\xi} : \mathbf{a}}{\|\boldsymbol{\xi}\|}. \quad (38)$$

The plastic part of the skew symmetric portion of the velocity gradient follows from a constitutive definition presented by Prantil [72] and is given by the expression

$$\mathbf{w}^p = \frac{1}{\lambda_g} (\mathbf{a}\mathbf{d}_p - \mathbf{d}_p\mathbf{a}) \quad (39)$$

where  $\lambda_g$  is a fitted constant associated with the angle between active slip systems. Bammann and Aifantis [60] proposed a similar form of the plastic spin based on the micromechanics of single slip. Other forms were proposed by Dafalias [95] and Loret [96] using representation theorem.

### 2.2.1. Anisotropy in the Isotropic Hardening

Next we consider the evolution equation of the state variables in the EMMI model. As a crystalline material deforms, the majority of hardening occurs on the slip systems most closely aligned with the maximum resolved shear stress. The farther the slip direction from the direction of the maximum resolved shear stress, the less the increases in hardening. Since the EMMI model, like many ISV models describe the storage and recovery processes associated with SSDs using a single scalar variable, the effect of hardening differences on different slip systems is not described. The coaxiality parameter is a measure of this effect in a continuous, rather than discrete manner. Hardening is a maximum when the structure tensor (texture from prior loading) aligns with the direction of current plastic flow and diminishes as the direction between the two increases. Textural effects are then incorporated into the isotropic hardening evolution equation in the following form:

$$\dot{\kappa} = ((1 - C)H + CH \cos(\bar{\eta}) - R_d \kappa) \dot{\epsilon}_p - R_s \kappa \sinh\left(\frac{Q_s}{2c_\kappa \mu} \kappa_s\right) \quad (40)$$

where  $H$ ,  $R_d$ , and  $R_s$  are constants associated with hardening, dynamic recovery, and static recovery moduli respectively,  $C$  is an anisotropic parameter ranging from 0 to .5 that describes the reduction in the isotropic hardening modulus related to the refinement of SSDs within the grain boundaries,  $\cos(\bar{\eta})$  is a coaxiality term describing the orientation of the direction of plastic deformation with respect to the orientation of previously developed texture defined as

$$\cos(\bar{\eta}) = \frac{\mathbf{a}'}{\|\mathbf{a}'\|} : \frac{\mathbf{d}_p}{\|\mathbf{d}_p\|} \quad (41)$$

where  $\mathbf{a}'$  is the deviatoric texture tensor and  $\mathbf{d}$  is the plastic stretch tensor. This modification is associated with the refinement of SSD structures within the grain boundaries exhibited in cyclicly loaded polycrystalline materials. This refinement of SSDs is associated with a reduction in the saturation stress when compared to uniaxially loaded specimens.  $\cos(\bar{\eta})$  ranges from -1 when the deformation is fully reversed from the direction of previously developed texture and when the deformation is monotonic with the direction of previously developed texture. When  $\cos(\bar{\eta})$  is equal to -1, it will impart

a reduction in the isotropic hardening modulus which results in a lowered saturation stress.

### 2.2.2. Anisotropy in the Kinematics Hardening

The backstress is an internal state variable associated with geometrically necessary dislocations and is a longer range stress describing misorientation between different grains or cells or the pile-up of dislocations at an obstacle. The evolution equation for the backstress is cast in hardening minus recovery format that is modified to account for anisotropy and is given by the equation

$$\dot{\boldsymbol{\alpha}} = \dot{\boldsymbol{\alpha}} - \mathbf{w}_e \boldsymbol{\alpha} + \boldsymbol{\alpha} \mathbf{w}_e = h(\eta) \mathbf{d}_p - r_d \dot{\boldsymbol{\epsilon}}_p \sqrt{\frac{2}{3}} \|\boldsymbol{\alpha}\| \boldsymbol{\alpha} \quad (42)$$

where  $r_d$  is a material constant associated with the dynamic recovery.  $h(\eta)$  is the kinematic hardening modulus that evolves due to textural effects. A heuristic form for the functional form of  $h(\eta)$  is postulated as:

$$h(\eta) = h \left( \exp(C_a (1 - |\cos(\eta)|)) + \exp(C_b \eta) \cdot 0.5 (1 - \cos(\eta)) + 0.5 (1 + \cos(\eta)) \right) \quad (43)$$

where  $h$  is the uniaxial kinematic hardening modulus.  $C_a$  is a scalar constant associated with cross loading and  $C_b$  is a scalar constant associated with textural effects.  $\eta$  is a scalar parameter describing textural effects which is given by the expression

$$\eta(\bar{\eta}) = C_1 \cos(\bar{\eta}) + C_2 \cos(2\bar{\eta}) + C_3 \cos(3\bar{\eta}) + C_4 \cos(4\bar{\eta}) \quad (44)$$

following an early suggestion of Regueiro et al. [71]. In Eq.(44) the parameters  $C_1, C_2, C_3$  and  $C_4$  are material constants that capture the shape change of the yield surface and are associated with the effects the respective orientation of texture has on the glide of dislocations.  $\bar{\eta}$  is the angle between the direction of plastic flow and the texture tensor.  $C_1$  is associated with the restriction or free movement of dislocations in monotonic and reverse loading respectively. This phenomenon will manifest itself as an increased translation of the apparent yield surface.  $C_2$  is associated with the development of dislocation structures orthogonal to the direction of texture which will impact the glide of dislocations on latent slip systems. This phenomena will present itself as an elongation of the apparent yield surface in cross loading or a sudden jump in

the flow stress in orthogonal load path changes.  $C_3$  is associated with additional effects on dislocation glide along previously activated slip systems and latent slip systems. This mixed effect is made apparent through a flattening of the apparent yield surface.  $C_4$  is associated with all higher order textural effects. When the deformation is monotonic with the direction of previously developed texture  $h(\eta)$  reduces to the uniaxial hardening modulus  $h$ . The degree in which  $\eta$  can contribute to the shape change of the yield surface is controlled by the parameter  $C_b$ .  $.5(1 - \cos(\bar{\eta}))$  has a maximum value of 2 when the specimen is loaded fully reversed from the direction of texture and a minimum value of 0 when the specimen is loaded monotonically with the direction of previously developed texture. The parameters  $C_1, C_2, C_3$  and  $C_4$  must be chosen to ensure  $\eta$  is zero in a full load reversal. The final term in  $h(\eta)$  ensures that it reduces to the uniaxial hardening modulus in monotonic and reversed loading conditions.

### 3. Results

In this section model predictions will be compared to the small strain offset yield surface data of Brown [26], in which yield is determined by probing stress space after various preloads. The model was implemented into Mathematica software as material point simulator by [97, 98]. Two cases will be considered: with the anisotropy terms in the flow rule and with the anisotropy terms in the evolution of the state variables. The precise steps employed by Brown were included in the simulations. After a prestrain, loading was simulated, from the new prestrain origin, in a direction in stress space until the 0.005 strain offset was reached. Then the material is unloaded back to the origin, followed by repetition of the process in a new direction. An alternate approach would be to ignore the effect of loading and unloading, and determine the parameters that give the best "fit" to the experimentally observed yield surface. The two approaches result in different sets of parameters and in matching the exact steps used in the experimental process. As an example of the normal method of "fitting" parameters of a flow surface to an experimentally defined surface in stress space, first consider the data of Stout [?]. The flow rule in EMMI is inverted resulting in a rate dependent flow surface and the four anisotropy parameters will be determined as a best match to the data

### 3.1. Case 1: Anisotropy in Flow Rule

The model is simplified following the assumption that temperature change in the material is negligible henceforth all thermally varying components are zero and the material remains at the initial temperature. In addition, we assume material anisotropy occurs in the direction of plastic deformation; therefore the coaxiality term remains at unity ( $\eta = 1.0$ ). This also implies that an isotropic material loaded uniaxially will not exhibit any anisotropy in any other direction. Based on these assumptions, an uniaxial stress-strain data is sufficient for identifying the parameters associated with the plastic part of the symmetric portion of the velocity gradient  $\mathbf{d}_p$ . This also hold true for the isotropic ( $\dot{\kappa}$ ) and kinematic ( $\dot{\alpha}$ ) hardening rates. The model is further simplified following the assumption that the static recovery contribution to the isotropic hardening rate is negligible ( $R_s = 0$ ).

From stability analysis of differential equations the efficient approach to integrating any system(s) of ordinary equations is an implicit time marching algorithm. An implicit time marching approach is efficient because larger time steps ( $\Delta t$ ) can be taken without compromising the numerical solution. The EMMI model equations are modified here to account for texture and anisotropy requires additional numerical considerations.

Numerical integration was performed using a material point simulator written in Mathematica 9 initially designed by [97, 98] to model multiphase materials. Without any consideration for texture and anisotropy, the flow rule can be evaluated by treating the effective plastic flow as either a function to be computed at every time step or as an additional evolution equation. With  $\eta$  incorporated into the net effective plastic flow there is an additional dependence on the plastic part of the symmetric portion of the velocity gradient which is directly dependent on the effective plastic flow, that is, the equation

$$\eta(\phi) = \hat{f}(\dot{\epsilon}_p) \quad (45)$$

where  $\hat{f}$  implies a functional. Therefore, the initial conditions for both plastic strain ( $\epsilon_p$ ) and plastic strain rate ( $\dot{\epsilon}_p$ ) have to be prescribed. This numerical caveats becomes

Parameter	Symbol	Value	Unit
$\dot{\kappa}$ -Equation			
Hardening	$H_{\kappa}$	11850	psi
Recovery	$R_d$	2.26	-
Recovery	$R_s$	0	1/s
Parameter	$Q_s$	1	-
Parameter	$C_s$	1	-
$\dot{\alpha}$ -Equation			
Hardening	$h_{\alpha}$	1.24E6	psi
Recovery	$r_d$	0.0245	-
Parameter	$C_a$	1	-
$\dot{\alpha}$ -Equation			
Parameter	$C_1$	2	-
Parameter	$C_2$	4	-
Parameter	$C_3$	2	-
Parameter	$C_4$	1	-
Parameter	$\lambda_g$	1.3E5	-
$\dot{\sigma}$ -Equation			
Yield Stress	$Y_0$	1700	psi
Shear Modulus	$\mu$	3.6E6	psi
Elastic Modulus	$E$	10E6	psi
Poisson's Ratio	$\nu$	0.3	-

Table 1: Material parameters for Aluminum 1100-O determined using multiple strain rate experimental data of Hockett [99] and Brown [26]. Anisotropic parameters were fitted to anisotropic data of specimen 06 in Brown [26]. The yield, shear, and elastic modulus are those reported in Brown [26].

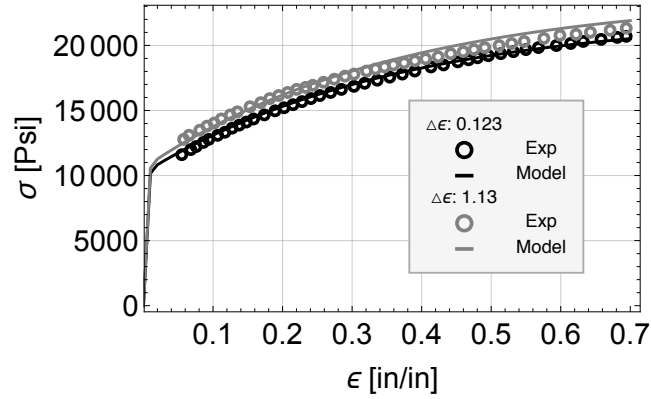


Figure 1: EMMI model parameters to fit to uniaxial compression data of Aluminum 1100-O [99]

important when implementing an either implicit or explicit integration algorithm for a material subroutine in ABAQUS [100] finite element code.

The initial yield stress was assumed to be the approximate stress that demonstrated a deviation from linearity in the uniaxial testing presented in Brown [26]. The uniaxial parameters were simultaneously fitted to uniaxial compression data presented by Hockett [99] taken at constant compression strain rates of  $\dot{\epsilon} = 0.123s^{-1}$  and  $\dot{\epsilon} = 1.13s^{-1}$  at room temperature and the small strain uniaxial data presented by Brown [26].

The uniaxial stress strain data presented by Hockett was performed via cam plastometer tests providing a constant axial compression deformation rate. Figure 1 is a plot comparing the fitted uniaxial model with multiple constant strain rate data of Aluminum 1100-O presented by Hockett [99]. Table 1 is a table listing all of the fitted parameters and relevant material properties for the model. The subsequent anisotropic yield surfaces of specimen 06 obtained by Brown [26] were then used to determine the additional anisotropic parameters  $C_1, C_2, C_3, C_4$  and  $\lambda_g$  to best capture the shape change and rotation of the yield surface. The initial isotropic yield surface of Aluminum 1100-O was determined by integrating equations 28, 13, 15 at a constant total stress rate of  $\dot{\sigma} = 85$  psi/min at 128 different evenly spaced loading directions in stress

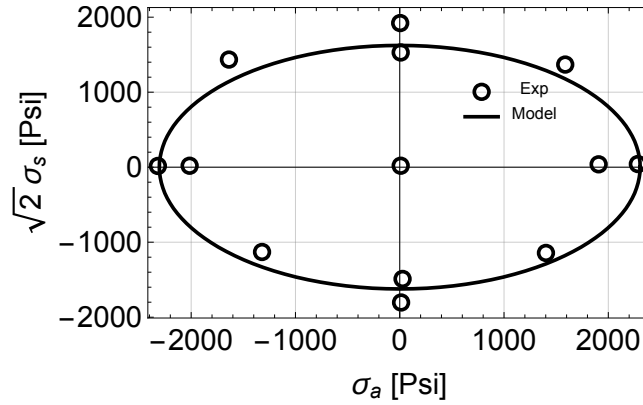


Figure 2: Initial isotropic yield surface of Aluminum 1100-O predicted by EMMI model and compared to the isotropic yield surface experimentally obtained by Brown [26]

space. The initial conditions for each of the integrated equations were set to zero in determination of the isotropic yield surface. Figure 2 is a plot comparing the model prediction of the initial isotropic yield surface to the initial isotropic yield surface presented in Brown [26].

The first inelastic state was used to determine the anisotropic parameters  $C_1, C_2, C_3, C_4$  which capture the shape change of the yield surface. The values of the internal state variables at the first preload point were determined by integrating equations 13, 15 and 28 in pure reverse shear to a preload state with the axial component  $\sigma_a = 0$  psi and shear component  $\sqrt{2}\sigma_s = -3353$  psi at a total constant stress rate of  $85$  *psi/min*. The initial conditions of the internal state variables were set to all values equal to 0 to replicate initial isotropic undeformed conditions. The internal state variables  $\kappa$  and  $\alpha$  at the end of the load step were then stored for yield surface calculation. The structure tensor  $\mathbf{a}$  is assumed to be fully evolved in the reverse shear direction, stemming from the assumption there was no existing anisotropy prior to the initial preload step.

The anisotropic yield surface for the first inelastic state was determined by integrating equations 28, 13, 15 from the experimentally obtained center of the yield surface

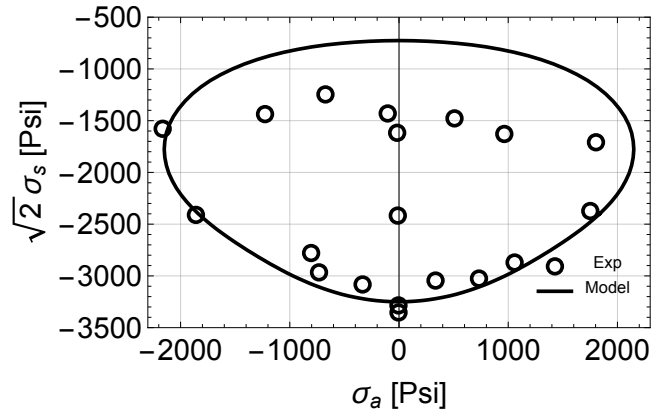


Figure 3: Comparison of experimentally obtained anisotropic yield surface of Aluminum 1100-O by Brown [26] to the anisotropic yield surface predicted by the model. Inelastic state of Aluminum 1100-O at a preload defined by an axial stress component  $\sigma_A = 0$  psi and shear stress component  $\sqrt{2}\sigma_s = -542$  loaded from an initially isotropic unloaded state

at the first inelastic state, with  $\sigma_a = 0$  ksi,  $\sigma_s = -2400$  ksi the axial and shear components of the center of the yield surface respectively. The internal state variables from the end of the first preload step are used as initial conditions for the respective evolution equations for integration from the center of the yield surface. To determine a yield point, equations 28, 13, 15 are then integrated in a specified load direction at a total stress rate of  $85 \text{ psi}/\text{min}$  until an accumulated equivalent plastic strain of 5 microstrain is achieved. The stress state at the prescribed offset is then stored as the yield stress and the process repeated for 128 evenly spaced load directions. Figure 3 is a plot comparing the predicted anisotropic yield surface from the model to the experimental data of the first inelastic state presented by Brown [26]. The model replicates the overall shape change of the yield surface quite well, characterized by the sharpening of the yield surface in the direction of the preload point and the flattening of the yield surface on the side opposite of the preload point. The model does slightly over-predict the curvature of the yield surface on the side opposite the preload point.

The state variables  $\kappa$ ,  $\alpha$  and  $\mathbf{a}$  at the second preload was determined by integrating equations 28, 20, 13, 15 from the first preload to the second preload defined by an axial and shear component of  $\sigma_A = 508$  ksi,  $\sigma_s = -3454$  ksi respectively, at a

constant total stress rate of  $85 \text{ psi}/\text{min}$ . The final values at the first preload point of the internal state variables  $\kappa$  and  $\alpha$ , the structure tensor  $\mathbf{a}$ , and the stress  $\sigma$  were used as the initial conditions of the respective evolution equations in the integration from the first preload point to the second preload point. The final state of  $\kappa$ ,  $\alpha$ , and  $\mathbf{a}$  at the end of the second preload step were stored and used as initial conditions for the integration of equations 28, 13, 15 in determination of each yield point of the second inelastic state. The material is not being loaded from an initially isotropic condition, therefore the structure tensor  $\mathbf{a}$  must be evolved with deformation from the first preload point to the second preload point, however it is assumed that the 5 microstrain in yield stress determination has little effect on the direction of anisotropy and the direction of anisotropy is held constant in the determination of the yield points in the yield surface determination. The anisotropic parameter  $\lambda_g$  is physically linked to the orientation of the active slip systems and controls the rate at which the structure tensor evolves towards the direction of deformation. The  $\lambda_g$  controls how rapidly the structure tensor reaches a steady state that is coaxial with the direction of plastic deformation.

The yield surface of the second inelastic state was determined in a similar manner as the yield surface of the first inelastic state: integrating equations 28, 13, 15 from the experimentally obtained center of the yield surface with axial and shear components  $\sigma_a = 525 \text{ ksi}$ ,  $\sigma_s = -2500 \text{ ksi}$  respectively. The values of  $\kappa$ ,  $\alpha$ , and  $\mathbf{a}$  at the end of the second preload step were used as initial conditions in the integration of equations 28, 13, 15 in the calculation of the yield stresses of the second inelastic state. Equations 28, 13, 15 were then integrated from the center of the yield surface in a prescribed stress direction with a total stress rate of  $85 \text{ psi}/\text{min}$  until an accumulated equivalent plastic strain of 5 microstrain was achieved and the stress at the 5 microstrain point was stored as the yield stress. The process was repeated for 128 evenly spaced load directions and the axial and shear components of the yield stresses plotted.

Figure 4 is a comparison of the experimental yield surface versus the yield surface predicted by the model of the second inelastic state. The experimental yield surface shows a rotation of the yield surface towards the direction of the preload accompanied

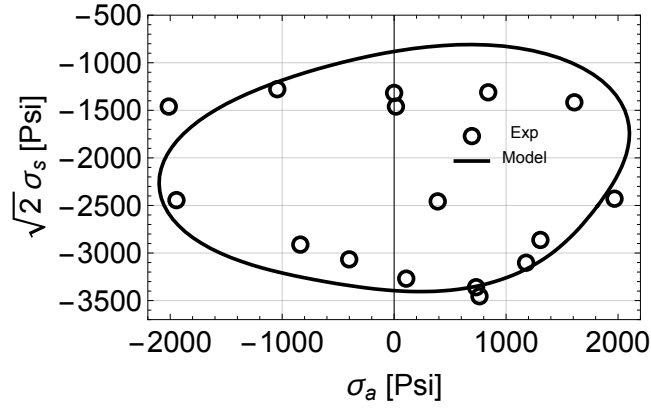


Figure 4: Comparison of experimentally obtained anisotropic yield surface of Aluminum 1100-O by Brown [26] to the anisotropic yield surface predicted by the model. Inelastic state of Aluminum 1100-O at a preload defined by an axial stress component  $\sigma_A = 508$  psi and shear stress component  $\sqrt{2}\sigma_s = -3454$  loaded from an initial preload defined by an axial stress component  $\sigma_a = 0$  psi and shear stress component  $\sqrt{2}\sigma_s = -3353$  psi

with a slight elongation of the yield surface to an egg shape, while the flattened side of the yield surface remains relatively unchanged. The rate at which the yield surface rotates is proportional to the anisotropic term  $\lambda_g$ , which physically describes the rate the underlying material anisotropy develops in the respective direction of loading. The model is able to replicate the overall rotation and elongation of the yield surface quite well, but predicts a different curvature on the side of the yield surface opposite of the preload point. The state of the variables  $\kappa$ ,  $\alpha$  and  $\mathbf{a}$  at the third preload was determined by integrating equations 28, 20, 13, 15 from the second preload to the final preload having values for the axial and shear components  $\sigma_a = 0$  ksi,  $\sigma_s = -542$  ksi at a constant total stress rate of 85 psi/min. The values of  $\kappa$ ,  $\alpha$  and  $\mathbf{a}$  at the end of the second preload step were used as initial conditions for the integration of their respective evolution equations from the second preload point to the third preload point.

The yield surface for the third step was determined in a similar fashion as the yield surface for the first and second inelastic states using the experimentally obtained yield surface center with axial and shear components  $\sigma_a = 0$  ksi  $\sigma_s = -1300$  ksi respec-

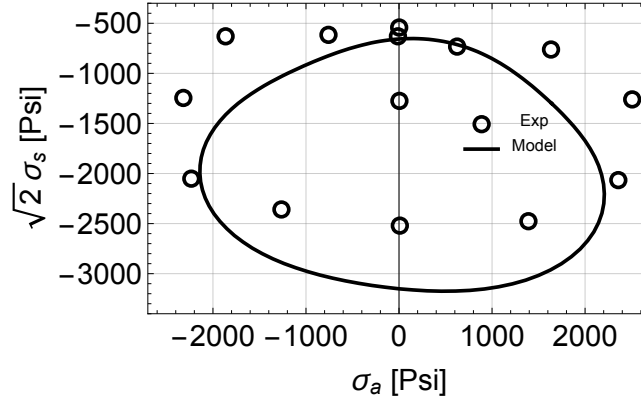


Figure 5: Comparison of experimentally obtained anisotropic yield surface of Aluminum 1100-O by Brown [26] to the anisotropic yield surface predicted by the model. Inelastic state of Aluminum 1100-O at a preload defined by an axial stress component  $\sigma_A = 0$  psi and shear stress component  $\sqrt{2}\sigma_s = -542$  loaded from an initial preload defined by an axial stress component  $\sigma_A = 508$  psi and shear stress component  $\sqrt{2}\sigma_s = -3454$  psi

tively. The values of  $\kappa$ ,  $\alpha$  and  $\mathbf{a}$  from the end of the third preload step were used as the initial conditions at the center of the yield surface corresponding to the third inelastic state. Equations 28, 20, 13, 15 were then integrated at 128 evenly spaced loading directions at a total stress rate of 85 psi/min until an accumulative equivalent plastic strain of 5 microstrain was achieved. Figure 5 is a plot comparing the prediction of the third inelastic state to the experimentally obtained yield surface. The experimental yield surface depicted a flattening of both the side of the yield surface facing the preload point and the side opposite the preload point. The model predicts the flattening of the side opposite the preload point, but predicts a slight sharpening of the yield surface near the preload point. The sharpening predicted by the model indicates the texture is developing in the positive shear direction even though the load point is still in the reverse shear region of stress space.

### 3.2. Case 2: Anisotropy in Evolution of State variables

Various uniaxial experimental observations exhibiting a form of anisotropic behavior that can be linked to either the development of texture or the development of anisotropic microstructural effects were replicated using the proposed model. Stainless

steel SS304 has been observed to exhibit a significant difference in hardening behavior when loaded in compression or torsion [101]. This difference in hardening behavior can be linked to the difference in the texture that develops during the different loadings. This phenomenon was successfully modeled by the plastic spin and the evolution of the structure tensor. The material was assumed to remain at constant temperature and any static recovery was ignored. The material parameters  $n, f, H, R_d, h, r_d$  were fitted to multiple strain rate data of SS304 presented in Bammann et al. [101]. The anisotropic parameter  $c$  and  $c_\alpha$  were assumed to be zero. The model equations were integrated at a constant strain rate in uniaxial compression and torsion, in which the initial values of the internal state variables were assumed to be 0. The anisotropic parameter  $\lambda_g$  was chosen to best simulate the difference in hardening behaviors. Figure 6 is a comparison of the model predictions of SS304 in uniaxial compression and torsion compared to the experimental findings presented in Bammann et al. [101]. The parameters for the model predictions are given in Table 2.

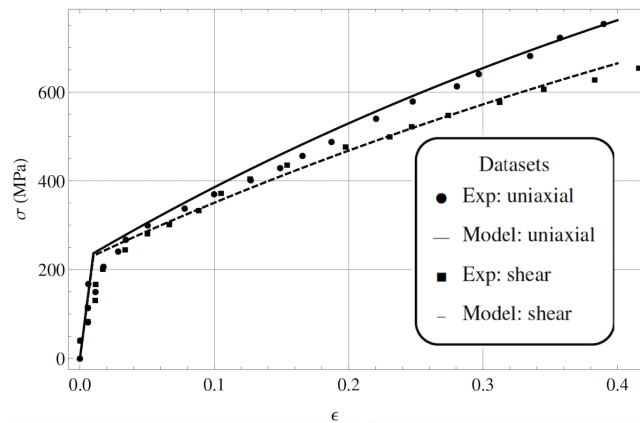


Figure 6: Model predictions of SS304 steel in compression and torsion. Model predictions of SS304 steel in uniaxial compression and torsion compared to experimental load data presented in Bammann et al. [101].

Large strain multidirectional compression simulations of 1100 Aluminum were

performed following the experimental data presented by Hockett and Sherby [30]. Due to the lack of reverse loading data, isotropic hardening is the only hardening mechanism considered. Isothermal conditions were assumed and static recovery was ignored. The hardening and dynamic recovery moduli  $H$  and  $R_d$  were fit to the large strain uniaxial compression data presented by Hockett and Sherby. The anisotropic parameters  $\lambda_g$  and  $c$  were fit via a trial and error process to the multidirectional compression data. Table 3 lists the values of the model parameters for Aluminum 1100.

Figure 7 illustrates the multidirectional compression tests which consist of incrementally straining a cubic specimen along each axis to a large total strain. This process was simulated by compressing along the global  $x_1$  axis the desired strain increment.

Parameter	Symbol	Value
Elastic Modulus	$E$	193000
Poisson Ratio	$\nu$	0.3
Yield Stress	$Y_0$	210
EMMI parameter	$n$	2.2
EMMI parameter	$f$	0.9
Hardening Parameter	$H$	1400
Recovery Parameter	$R_d$	1.2
Recovery Parameter	$R_s$	0
Parameter	$Q_s$	0
Parameter	$C_s$	0
Hardening	$h$	0
Recovery	$r_d$	0
Anisotropic	$\lambda_g$	40
Anisotropic	$C$	0
Anisotropic	$C_a$	0

Table 2: Model parameters for SS304

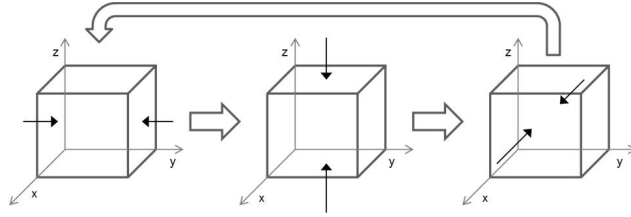


Figure 7: Incremental multidimensional compression test schematic. Schematic illustrating the incremental multidimensional compression test performed by Armstrong et al. [30]. Cube specimens were loaded along a single specimen the desired strain step. The specimens were then rotated 90 degrees and loaded in compression the desired strain step. The specimen is then rotated 90 degrees and compressed along the third axis. The process is repeated until the desired total compressive strain is achieved.

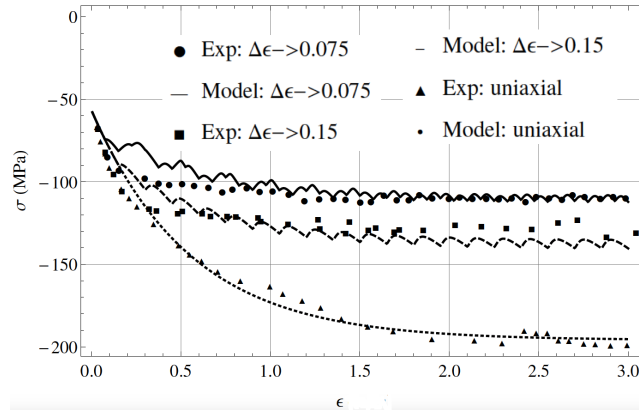


Figure 8: Model predictions for uniaxial and multidirectional compression data of aluminum 1100 compared to experimental data from Armstrong et al. [30]

The state variables at the end of the compression step become the initial conditions in the next strain step. Prior to the next strain step the tensorial variables were rotated  $-90$  degrees around the global  $x_1$  axis, followed by a rotation of  $-90$  degrees around the global  $x_2$  axis aligning a new material axis in the global  $x_1$  direction. The process was repeated until the final total strain was achieved. A strain rate of  $-0.005s^{-1}$  was used for all simulations, and two strain increments were used for multidirectional compression simulations  $d\epsilon = -0.075$ ,  $d\epsilon = -0.15$  to a total strain of  $-3.2$ .

Armstrong et al. [30] observed a directional softening or a reduction in saturation stress with multidirectional compression compared to uniaxial compression. The

Parameter	Symbol	Value
Elastic Modulus	E	64000
Poisson Ratio	$\nu$	0.3
Yield Stress	$Y_0$	34
EMMI parameter	n	13.2
EMMI parameter	f	$2.36 \times 10^{-7}$
Hardening	H	122.7
Recovery	$R_d$	1.48
Recovery	$R_s$	0
Parameter	$Q_s$	1
Parameter	$C_s$	1
hardening	h	0
recovery	$r_d$	0
Anisotropic	$\lambda_g$	11
Anisotropic	C	0.62
Anisotropic	$C_a$	0

Table 3: Fitted model parameters for Aluminum 1100 at room temperature.

difference in saturation stresses can be attributed to the directional dependence of the microstructure that forms during each increment of loading. Multidirectional compression specimens were found to reach a stable grain and subgrain concentration at a strain of  $-1.6$  and little to no dislocation entanglements and substructures within the boundaries at a strain of  $-3.2$ . The uniaxial specimen never achieved a stable grain and subgrain concentration and was found to have dislocation entanglements and substructures within the boundaries up to strains of  $-3.2$ . The magnitude of the saturation stress also exhibited a dependence on the size of the incremental strain step. The modified isotropic hardening evolution equation was able to capture this behavior reasonably well, Figure 8 is a plot of the saturation stress for the uniaxial simulation and multidirectional compression simulations with strain steps of  $0.075$  and  $0.15$ . The model was not able to capture the initial knee from the short transient, this behavior could possibly be captured by including the short transient backstress. The magnitude of the saturation stress for each strain increment is controlled by how rapidly the structure tensor aligns with the direction of plastic flow, which is captured through the coaxiality term  $\eta$ . When the structure tensor and plastic flow are not aligned, the coaxiality term is less than 1 ( $\eta < 1$ ) which results in a reduction in the saturation stress. When the coaxiality term is 1, the structure tensor and direction of plastic flow are aligned and there is no reduction in the isotropic hardening modulus. This phenomenon is representative of the underlying texture and microstructure aligning in the direction of uniaxial deformation. The rate at which the coaxiality term approaches 1 is proportional to the anisotropic parameter  $\lambda_g$ , Figure 9 is a plot of  $\eta$  for three strain steps of  $d\epsilon = 0.15$  with various values for  $\lambda_g$ . The anisotropic parameter  $c$  describes the degree of anisotropic behavior exhibited in the isotropic hardening and sets a limit to the reduction  $\eta$  can impart on the isotropic hardening modulus. The parameter  $c$  is bounded such that  $0 \leq c \leq 1$ . Tests were also performed in which the specimen was initially uniaxially deformed to a strain of  $-1.6$  followed by multidirectional compression with a strain increment of  $d\epsilon = 0.15$  as well as multidirectional compression to a strain of  $-1.6$  followed by uniaxial compression. The specimens initially under uniaxial loading conditions were found to approach a larger saturation stress upon multidirectional loading compared to the specimen that solely underwent multidirectional compression. This

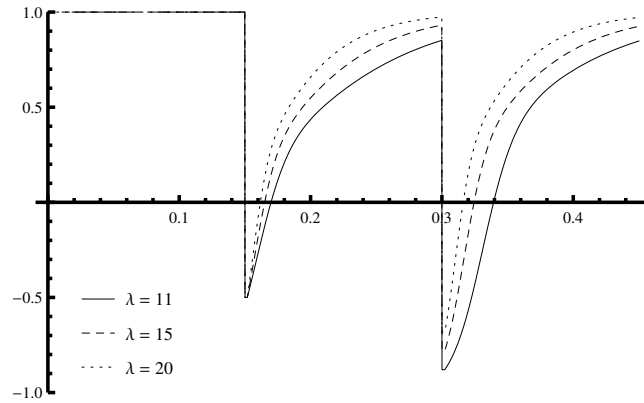


Figure 9: evolution of the coaxiality term over three strain steps of multidirectional compression with a strain step of 0.15 and various  $\lambda_g$

discrepancy in saturation stresses is attributed to a significantly larger amount of dislocation entanglements compared to the specimens experiencing only multidirectional compression to a lesser total strain. Figure 10 is a plot of the model following these same loading conditions, in which the model is able to replicate the softening behavior but the discrepancy in the saturation stress is not captured as well. A slight adjustment in  $\lambda_g$  parameter matches the behavior exactly, Figure 11 is a plot of the same loading conditions with a slightly larger  $\lambda_g$ . This suggests the parameter  $\lambda_g$  may evolve, or this effect may be related to a Bauschinger effect and might be described with kinematic hardening. Shear to uniaxial compression load path changes were simulated following experimental data presented by Dawson and Follansbee [102]. An OFHC plate with an initially tapered thickness was rolled to a constant thickness producing a specimen with varying amounts of rolling reduction along the direction of the taper. The variation in the rolling reduction resulted in spatially varying mechanical properties. Compression specimens were machined from the rolled plate with the compression axis parallel to the rolling direction and uniaxial compression tests were performed on specimens with various amounts of shear prestrain (rolling reduction). The amount of rolling reduction of each compression specimen can be calculated based on the distal location from the thickest end of the taper in which the specimens were machined. Loading the specimens in compression is representative of a sudden load path change from shear to

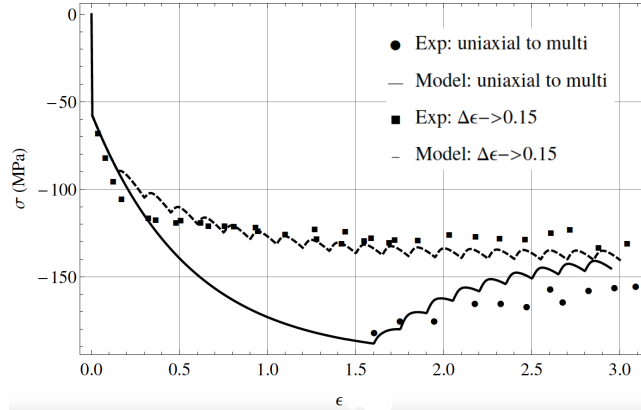


Figure 10: Model predictions of multidirectional compression and uniaxial compression to a strain of 1.6 followed by multidirectional compression with a strain step of 0.15 and  $\lambda_g = 11$ . Model predictions compared to experimental data presented by Armstrong et al. [30]

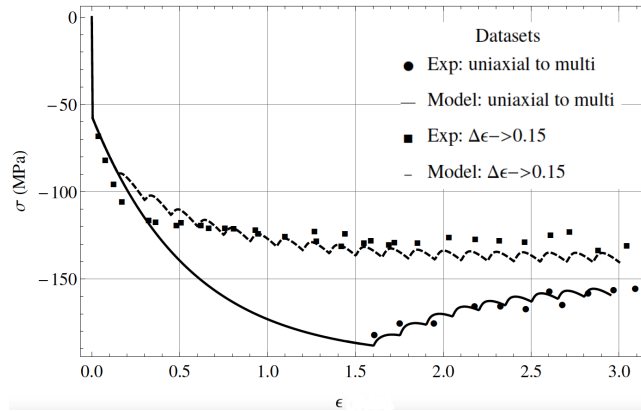


Figure 11: Incremental multidirectional to uniaxial compression data with various  $\lambda_g$  parameters. Model predictions of multidirectional compression and uniaxial compression to a strain of 1.6 followed by multidirectional compression with a strain step of 0.15 and  $\lambda_g = 11$  for multidirectional only simulation and  $\lambda_g = 15$  for the uniaxial followed by multidirectional compression. A slight increase in the parameter  $\lambda_g$  can predict the discrepancy in saturation stresses between the multidirectional and uniaxial to multidirectional compression tests. Model predictions compared to experimental data presented by Armstrong et al. [30].

uniaxial compression. The results of the uniaxial loading experiment of the study are assumed to be representative of the behavior of the material at a point. The initially rolled compression specimens were observed to rapidly exhibit uniaxial compression yield behavior at an equivalent strain upon uniaxial compression loading, suggesting a rapid evolution of the back stress.

The constants  $H$ ,  $R_d$ ,  $h$ ,  $r_d$ ,  $n$ ,  $f$  were fitted from uniaxial load reversal data presented by Miller et al. [101] and large strain compression data taken from Hockett and Sherby [103]. The data from Miller et al. [101] provided a mean to fit the hardening and recovery parameters while the large strain multiple rate compression data from Follansbee and Sherby provided a mean to fit the rate sensitivity parameters. Isothermal conditions were assumed and static recovery was ignored. The anisotropic parameters  $C_\alpha$  and  $\lambda_g$  were chosen to best fit the rapid change from shear to uniaxial compression using a trial and error process. Table 4 lists the model parameters for OFHC Copper. The pre-rolling reduction was determined by integrating the model equations in plane strain compression with the initial conditions of the internal state variables assumed to be zero.

Integration was performed using the Mathematica's NDSolve solver. The values of the internal state variables at the end of the preload step were then stored and used as initial conditions for the integration of the model equations in uniaxial compression. Figure 12 is the experimental data from Dawson and Follansbee [102] compared to the model predictions with  $C_\alpha = 1.8$  and the material parameter  $\lambda_g = 150$ . The modified form of the kinematic hardening evolution equation accounts for this rapid change through the exponential dependence in the coaxiality term. With the onset of uniaxial compression the coaxiality term  $\eta$  will be negative due to the difference in direction of the plastic deformation and the anisotropy developed from the rolling preload step. The negative coaxiality term will impart a rapid increase in the kinematic hardening modulus due to its exponential dependence on the coaxiality term. As the orientation of the anisotropy approaches the direction of plastic flow the exponential term reduces to 1 causing the kinematic hardening modulus to return to its original

isotropic value. Similar to the modified isotropic hardening evolution equation, how rapidly the hardening modulus saturates is dependent on how quickly the structure tensor aligns with the direction of plastic flow and is controlled by the  $\lambda_g$  parameter. Figure 13 is the experimental data from Dawson and Follansbee [102] compared to the model predictions with the parameter  $C_\alpha = 0$ . This selection of the parameter  $C_\alpha$  forces the exponential term in the modified kinematic hardening evolution equation to remain 1, essentially removing the rapid increase in the kinematic hardening from anisotropy, resulting in a less accurate prediction. In the following, model predictions will be compared to the small strain offset yield surface data of Brown [26], in which yield is determined by probing stress space after various preloads. Two cases will be considered: with the anisotropy terms in the flow rule and with the anisotropy terms in

Parameter	Symbol	Value
Elastic Modulus	E	41200
Poisson Ratio	$\nu$	0.3
Yield Stress	$Y_0$	40.2
EMMI parameter	n	6
EMMI parameter	f	0.2
Hardening	H	700
Recovery	$R_d$	2.6
Recovery	$R_s$	0
Parameter	$Q_s$	1
Parameter	$C_s$	1
hardening	h	1500
recovery	$r_d$	0.093
Anisotropic	$\lambda_g$	150
Anisotropic	C	0
Anisotropic	$C_a$	1.8

Table 4: Model parameters for OFHC Copper.

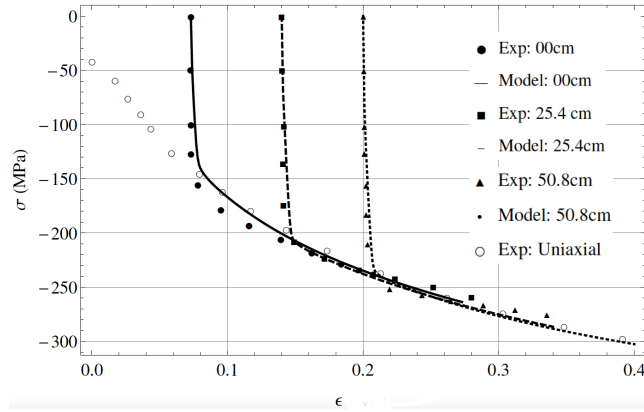


Figure 12: Model predictions using modified back stress evolution equations with  $c_{\alpha} = 1.6$  and  $\lambda_g = 150$ . Model predictions compared to RDCR data taken from Dawson and Follansbee [102] and large strain uniaxial compression data taken from Follansbee and Kocks [104]

the evolution of the state variables. In both cases, the precise steps employed by Brown were included in the simulation. After a prestrain, loading was simulated, from the new prestrain origin, in a direction in stress space until the  $0.005$  strain offset was reached. Then the material is unloaded back to the origin, followed by repetition of the process in a new direction. An alternate approach would be to ignore the effect of loading and unloading, and determine the parameters that give the best "fit" to the experimentally observed yield surface. The two approaches result in different sets of parameters and in matching the exact steps used in the experimental process, the resulting surface is not a sharply defined. As an example of the normal method of "fitting" parameters of a flow surface to an experimentally defined surface in stress space, first consider the data of Stout [?]. The flow rule in EMMI is inverted resulting in a rate dependent flow surface and the four anisotropy parameters will be determined as a best match to the data.

### 3.3. Anisotropy in the Flow Rule vs. Evolution of State Variables

We address the comparison of including the effects of anisotropy in the flow rule versus inclusion in the equations describing the evolution of state variables (which we shall label ISV model). The ISV model is then integrated using the same loading path as used by Brown [26] and a yield surface is determined by using the same 5 microstrain

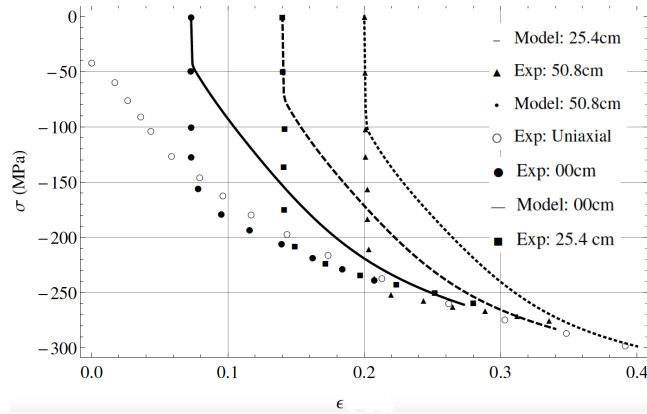


Figure 13: Model predictions without exponential term in back stress evolution equation. Predictions compared RDCR compression data taken from Dawson and Follansbee [102] and uniaxial compression data taken from Follansbee and Kocks [104]

offset definition as in the experiments. The uniaxial parameters  $H$ ,  $R_d$ ,  $h$ ,  $r_d$ ,  $f$ ,  $n$  and  $Y_0$  were fitted to uniaxial compression data of Aluminum 1100 presented by Hockett [99].

Table 5 is a table listing the best fit uniaxial parameters for Aluminum 1100. The anisotropic parameters  $C_1$ ,  $C_2$ ,  $C_3$ ,  $C_4$ ,  $C_a$ ,  $C_b$ ,  $C$  and  $\lambda_g$  were chosen to best replicate the distortion and rotation hardening exhibited in the experimental yield surfaces obtained by Brown [26]. Table 6 lists the anisotropic parameters for Aluminum 1100. The shear and elastic modulus were assumed to be equivalent to the values recorded by Brown [26]. This approach is similar to that used in Miller et al. [62] where the center of a small yield surface moved rapidly ahead of the load point and apparent yield consisted of the stress when the load point and yield surface coincide. The following figures illustrate that either approach results in very similar apparent yield surface and both compare favorably with the experimental data. Both models result in a distorted yield surface pointing in the direction of preload. The model assuming a static yield surface is able to capture the sharpening slightly better, however the anisotropic parameters for both models were fitted using a trial and error technique. It is possible that using an optimization algorithm to fit all of the model parameters will result in nearly identical model predictions. Another consideration is the large degree of uncertainty

associated with the experimental data. It is relatively difficult to acquire stress strain data at strains as small as 5 microstrain, and it can be assumed there is a rather large margin of error in the experimental data. To model the yield surface data using the ISV approach, the internal state variables are then integrated over the same load path as in the experiments to best replicate the change of state due to the probing process. To determine the initial values of the model equations in the yield surface determination, the model equations were integrated from the previous preload point to the respective preload. Table 7 lists the axial and shear components of the preload and the respective yield surface center. All integration was performed at a constant total stress rate of 85 Psi/min and it is assumed the unloading from the preload to the yield surface center has negligible effect on the internal state variables. To replicate the probing process, the

Parameter	Symbol	Value
Hardening Modulus	H	11850
Dynamic Recovery	$R_d$	2.26
Static Recovery	$R_s$	0
Parameter	$Q_s$	1
Parameter	$C_s$	1
Hardening Modulus	h	$1.24 * 10^6$
Dynamic Recovery	$r_d$	0.0254
Parameter	$C_a$	1
Rate Sensitivity	$n$	9.42
Rate Sensitivity	f	.000972
Initial Yield Stress	$\sigma_y$	1700
Shear modulus	$\mu$	$3.6 * 10^6$
Modulus of elasticity	E	$10 * 10^6$
Poisson ratio	$\nu$	.3

Table 5: Uniaxial model parameters of Aluminum 1100-O. Uniaxial material parameters for Aluminum 1100-O fit to multiple strain rate data presented by Hockett [99] and uniaxial small strain data in Brown [26].

model equations were integrated from the respective yield surface center until a desired offset strain was achieved. The process was repeated in 128 evenly spaced loading directions in order to generate a smooth representative yield surface.

Figure 15 is a plot comparing the anisotropic yield surface of Aluminum 1100-O for the second inelastic state predicted by both the model assuming a static yield surface presented in [105] and the model assuming an apparent yield surface presented in [105]. Both models captured the rotation of the distorted yield surface to point in the direction of preload, and the rotational hardening was controlled by the parameter  $\lambda_g$  in both models. Upon visual inspection, the model assuming an apparent yield surface captures the overall shape of the experimental data slightly better. Differences in the model predictions might be attributed to differences in model behavior or the trial and error parameter fits.

Figure 16 is a plot comparing the anisotropic yield surface of Aluminum 1100-O

Parameter	Symbol	Magnitude
Anisotropic parameter	$C_1$	-0.2
Anisotropic parameter	$C_2$	-0.8
Anisotropic parameter	$C_3$	0.8
Anisotropic parameter	$C_4$	0.2
Anisotropic parameter	$\lambda_g$	90000
Anisotropic parameter	$C$	0
Anisotropic parameter	$C_a$	
Anisotropic parameter	$C_b$	14

Table 6: Anisotropic model parameters for Aluminum 1100-O. Anisotropic parameters of Aluminum 1100-O fit to anisotropic yield surfaces presented by Brown [26]

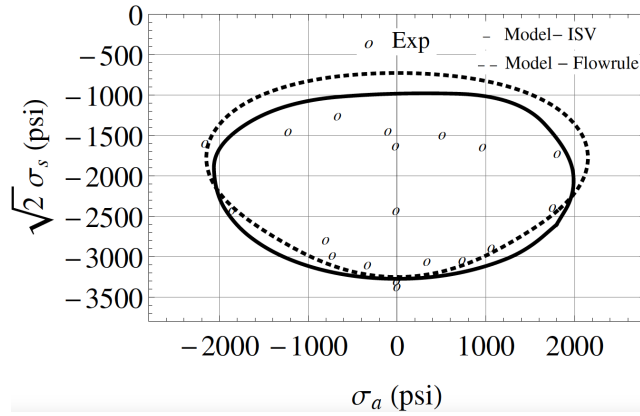


Figure 14: Model comparison at first inelastic state. Plot comparing the anisotropic yield surface of Aluminum 1100-O for the first inelastic state predicted by both the model assuming a static yield surface presented in [105] and the model assuming an apparent yield surface presented in [105]. Experimental data from Brown [26].

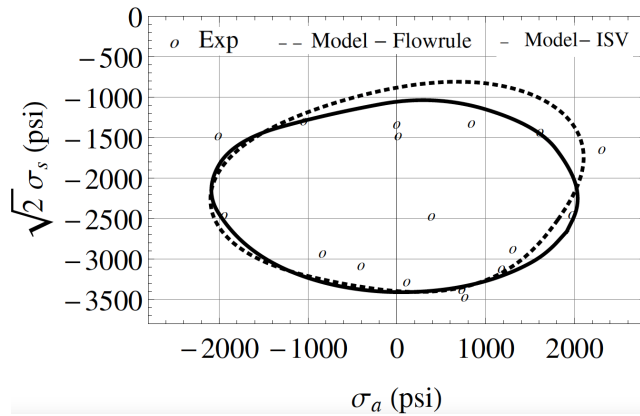


Figure 15: Model comparison at second inelastic state. Plot comparing the anisotropic yield surface of Aluminum 1100-O for the second inelastic state predicted by both the model assuming a static yield surface presented in [105] and the model assuming an apparent yield surface presented in [105]. Experimental data from Brown [26].

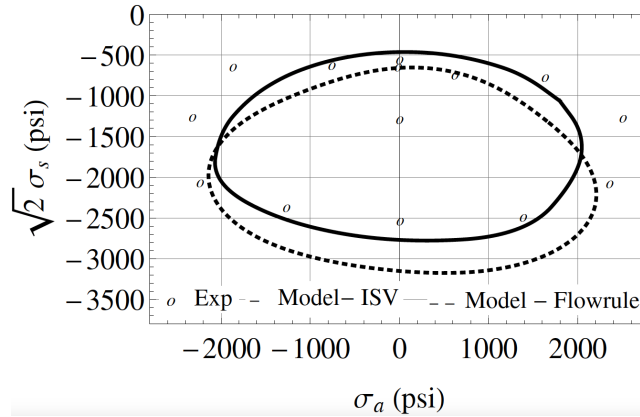


Figure 16: Model comparison at third inelastic state. Plot comparing the anisotropic yield surface of Aluminum 1100-O for the third inelastic state predicted by both the model assuming a static yield surface (flow rule) and the model assuming an apparent yield surface. Experimental data from Brown [26].

Inelastic State	Axial Preload	Shear Preload	Axial Center	Shear Center
initial	0	0	0	0
1	0	-3353	0	-2400
2	508	-3454	525	-2500
3	0	-542	0	-1300

Table 7: Axial and shear components of the preload and the respective yield surface center.

for the third inelastic state predicted by both the model assuming a static yield surface presented in both the model assuming a static yield surface (flow rule) and the model assuming an apparent yield surface (ISV). Both models capture the shift in direction of the distorted yield surface to point in the direction of positive shear. The differences in yield surfaces predicted by each model is most apparent at the third inelastic state. The apparent yield surface captures more of the experimental data while the fixed yield surface model captures more of a bullet shaped yield surface. Considering the possibility for experimental error in the experimental results, both models were able to replicate the anisotropic yield behavior of Aluminum 1100-O reasonably well. The model presented in [105] generates a static yield surface that is dependent on the definition of

yield. The model presented in [105] produces an apparent yield surface as a result of a small yield surface rapidly translating in stress space. This model is capable of producing an apparent yield surface for any offset strain definition of yield.

#### 4. Qualitative assessment of the model with texture effects

Accounting for textural evolution in a material model is important because a realistic material response is necessary for a more accurate prediction. In an effort to test the efficacy of the EMMI model with textural evolution we perform a multi-load numerical experiment where by we specify a piecewise and distinct loading condition in between a specified time interval.

The simulations were performed using [97, 98] numerical implementation of the model. In these simulations, we turn on and off the differential equation responsible for textural evolution Eq. 20. Conceptually, we start by simulating a rolling process. We then proceed by undoing some of the rolling and rapidly following that up with a shearing of the specimen. Herein, we believe that a model that accounts for textural evolution must capture the effects of the partial unrolling which creates a non-uniformly aligned material.

For Stage 1, we load the specimen in tension by specifying a positive magnitude for  $l_{2,2}^1 = 0.5/s$  component and therefore for volume preserving deformation we specify a negative magnitude on the  $l_{1,1}^1 = -0.25/s$  and  $l_{3,3}^1 = -0.25/s$  components. The index zero e.g.  $l_{2,2}^0$  indicates  $l_{2,2}$  for stage zero of the numerical experiment. For Stage 2, we load the specimen in compression with  $l_{2,2}^2 = -0.9/s$ , and therefore for volume preserving deformation we specify a positive magnitude in the  $l_{1,1}^2 = 0.05/s$  and  $l_{3,3}^2 = 0.05/s$  components. For stage 3, we load the specimen in shear by specifying a  $l_{1,2}^3 = 0.6/s$  component of the velocity gradient.

To proceed, we integrate the constitutive equations of the model while driving the deformation with the differential equation responsible for updating the state of the material

$$\dot{\mathbf{F}} = \mathbf{L}\mathbf{F}. \quad (46)$$

We replace the elastic symmetrical and anti-symmetrical portions (abbreviated by Sym

and ASym, respectively) of the velocity gradient in the equations of interest with:

$$\mathbf{d}_e = \text{Sym}(\dot{\mathbf{F}}\mathbf{F}^{-1}) - \mathbf{d}_p \quad \text{and} \quad \mathbf{w}_e = \text{ASym}(\dot{\mathbf{F}}\mathbf{F}^{-1}) - \mathbf{w}_p \quad (47)$$

Figure 17 and 18 show the material response and corresponding plastic flow for all pertinent components of the deviatoric portion of the Cauchy stress tensor and flow rate tensor with and without accounting for textural evolution. As shown, intuitively we expect less plastic flow (fig. 18b) in transition region from Tension-Compression to Shear relative to the case where material texture is not accounted for. This is due to the mechanically induced non-uniform texture in the material.  $dp_{1,1}$  (fig. 18a) of the plastic flow components shows an increased plastic flow in the aforementioned region and hence a corresponding increase material response. In addition, there is also less plastic flow in the  $dp_{2,2}$  relative to the  $dp_{1,1}$  as the non-uniformity was predominantly introduced in the  $dp_{2,2}$  component of the velocity gradient.

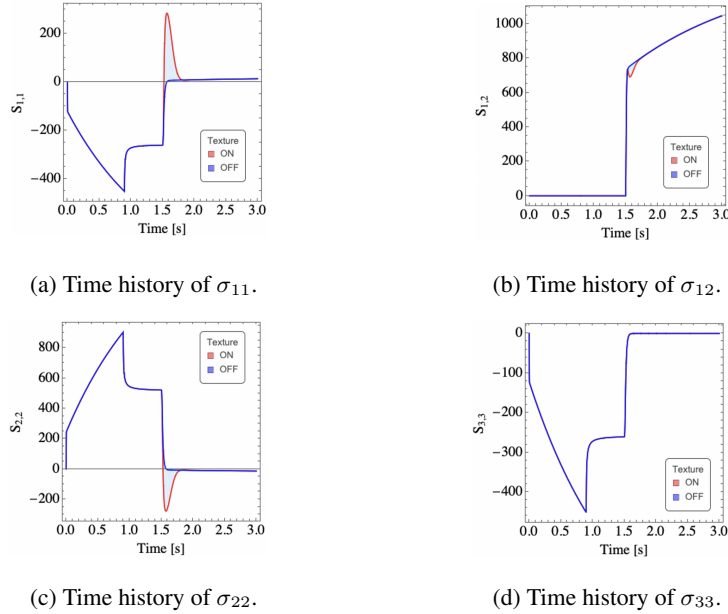


Figure 17: Material response for the cases with and without textural effects. The load is a tension followed by a compression and shear. Significant component of the Cauchy stress tensor were presented.

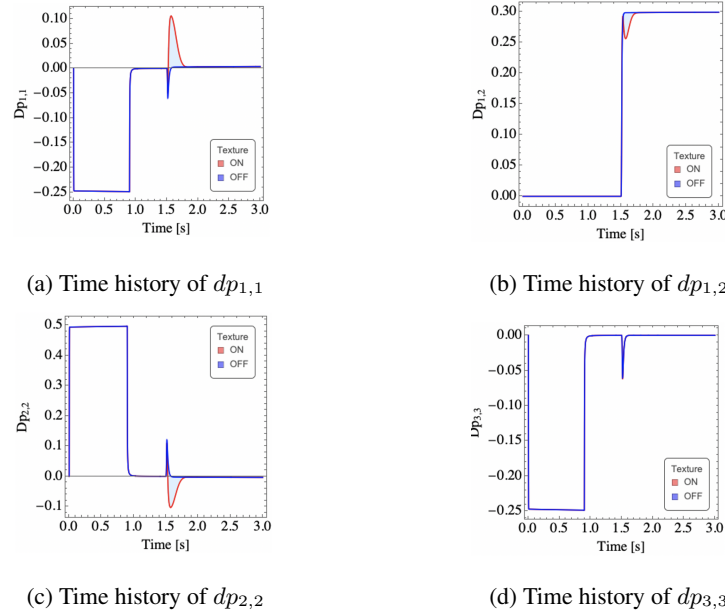


Figure 18: Flow rate histories for the cases with and without textural effects. The load is a tension followed by a compression and shear. Significant components of the flow rate tensor are displayed.

## 5. Conclusion

The Evolving Microstructural Model of Inelasticity (EMMI) [86] was modified to account for evolving anisotropy in addition to the normal anisotropy associated with kinematic hardening. Anisotropy was characterized by a second order orientation tensor, resulting from the truncation of the orientation distribution function (ODF) associated with texture, to second order. This tensor is key to the equation for the plastic spin (skew symmetric part of the plastic velocity gradient). In addition, the structure tensor was incorporated into the flow rule of EMMI (an existing rate and temperature dependent physically based plasticity model) via a scalar variable describing the coaxiality of the structure tensor with the direction of the rate of plastic deformation. This coaxiality term scales the isotropic hardening variable in the flow rule representing a prediction of crystal plasticity models such that hardening is decreased if the direction of plastic flow continues in the same (or nearly the same) direction of previous inelastic flow. The closure properties associated with the truncation of the ODF series to second or-

der Advani and Tucker [75] yield a prescribed evolution equation for the second order structure tensor. These modifications to the model were compared with experimentally obtained anisotropic yield surfaces of Aluminum 1100-O by Brown [26]. Using a five microstrain offset yield definition, Brown probed various inelastic states of a specimen at a prescribed preload by experimentally determining the respective yield surface of the specimen. The anisotropic parameters of the model were fitted to replicate the evolution of the first three anisotropic yield surfaces of specimen 06 presented by Brown. The predictions of the model compared favorably with the yield surfaces observed by Brown [26], predicting similar shape changes and rotations of the flow surfaces after various preloads.

The equations describing the evolution of the internal state variables were modified using the coaxiality factor. This includes the history effect due to the current direction of loading compared to previously hardened state of the material. This simulates the effect in crystal plasticity that slip systems closest to the direction of the maximum resolved shear stress harden more than those that are not closely aligned. This incorporated history effect was compared with the observed differences in the effective stress strain curves in torsion and compression, the shape of the reverse loading curve in copper and finally a complex set loading experiments on AL 1100-O exhibiting the large softening effects resulting from many load path direction changes. Once the again the model predictions compared very favorably with the observed data.

Finally, we address the issue of evolving state vs current state. In the first part we modified the current value of the state variables and compared this effect on the flow surface in the prediction of anisotropic yield surfaces after various preloads. Secondly, we modified the evolution of state and compared with various large strain experiments. Finally, we attempted to predict the yield surface changes by using only the modified evolution of state equations and the same small strain definition of yield as used in the experiments. The results were surprisingly good. Even though the predictions were probably within experimental error, the rapid changes in the direction of plastic flow associated with the normal to the sharpened corner yield surfaces predicted by

the modified flow rule, may be critical in the prediction of shape changes as well as localization phenomena. This will be addressed in a future work, along with developing a method to initialize the structure tensor based upon the texture of the material.

## **6. Acknowledgment**

The authors acknowledge the following institutions at Mississippi State University for their support of this work: (1.) Bagley College of Engineering (2.) The Department of Mechanical Engineering (3.) The Center for Advanced Vehicular Systems.

## References

- [1] P. Dawson, S. MacEwen, P. Wu, Advances in sheet metal forming analyses: dealing with mechanical anisotropy from crystallographic texture, *International Materials Reviews* 48 (2) (2003) 86–122.
- [2] D. Peirce, R. Asaro, A. Needleman, An analysis of nonuniform and localized deformation in ductile single crystals, *Acta metallurgica* 30 (6) (1982) 1087–1119.
- [3] R. Becker, J. Butler, H. Hu, L. Lalli, Analysis of an aluminum single crystal with unstable initial orientation (001)[110] in channel die compression, *Metallurgical Transactions A* 22 (1) (1991) 45–58.
- [4] R. Becker, Analysis of texture evolution in channel die compression - i. effects of grain interaction, *Acta metallurgica et materialia* 39 (6) (1991) 1211–1230.
- [5] K. K. Mathur, P. R. Dawson, On modeling the development of crystallographic texture in bulk forming processes, *International Journal of Plasticity* 5 (1) (1989) 67–94.
- [6] U. Kocks, Constitutive relations for slip, *Constitutive Equations in Plasticity*. Massachusetts Institute of Technology Press, Cambridge. 1975, 81-115.
- [7] U. Kocks, Constitutive behavior based on crystal plasticity, in: *Unified constitutive equations for creep and plasticity*, Springer, 1987, pp. 1–88.
- [8] F. Roters, P. Eisenlohr, L. Hantcherli, D. D. Tjahjanto, T. R. Bieler, D. Raabe, Overview of constitutive laws, kinematics, homogenization and multiscale methods in crystal plasticity finite-element modeling: Theory, experiments, applications, *Acta Materialia* 58 (4) (2010) 1152–1211.
- [9] P. Van Houtte, J. Gawad, P. Eyckens, B. Van Bael, G. Samaey, D. Roose, A full-field strategy to take texture-induced anisotropy into account during fe simulations of metal forming processes, *JOM Journal of the Minerals, Metals and Materials Society* 63 (11) (2011) 37–43.

- [10] G. Taylor, Plastic strain in metals. *jnl. inst. metals* (1938) 62, 307; the mechanism of plastic deformation of crystals, in: *Proc.*
- [11] G. I. Taylor, The mechanism of plastic deformation of crystals. part i. theoretical, *Proceedings of the Royal Society of London. Series A, Containing Papers of a Mathematical and Physical Character* 145 (855) (1934) 362–387.
- [12] G. I. Taylor, The mechanism of plastic deformation of crystals. part i. theoretical, *Proceedings of the Royal Society of London. Series A, Containing Papers of a Mathematical and Physical Character* 145 (855) (1934) 362–387.
- [13] J. Bishop, R. Hill, Cxxviii. a theoretical derivation of the plastic properties of a polycrystalline face-centred metal, *The London, Edinburgh, and Dublin Philosophical Magazine and Journal of Science* 42 (334) (1951) 1298–1307.
- [14] R. Hill, The elastic behaviour of a crystalline aggregate, *Proceedings of the Physical Society. Section A* 65 (5) (1952) 349.
- [15] A. Hershey, The plasticity of an isotropic aggregate of anisotropic face-centered cubic crystals, *Journal of Applied Mechanics-Transactions of the Asme* 21 (3) (1954) 241–249.
- [16] F. Barlat, J. W. Yoon, O. Cazacu, On linear transformations of stress tensors for the description of plastic anisotropy, *International Journal of Plasticity* 23 (5) (2007) 876–896.
- [17] F. Barlat, H. Aretz, J. Yoon, M. Karabin, J. Brem, R. Dick, Linear transformation-based anisotropic yield functions, *International Journal of Plasticity* 21 (5) (2005) 1009–1039.
- [18] F. Barlat, J. Brem, J. Yoon, K. Chung, R. Dick, D. Lege, F. Pourboghrat, S.-H. Choi, E. Chu, Plane stress yield function for aluminum alloy sheets part 1: theory, *International Journal of Plasticity* 19 (9) (2003) 1297–1319.
- [19] J. Yoon, R. Dick, F. Barlat, A new analytical theory for earing generated from anisotropic plasticity, *International journal of plasticity* 27 (8) (2011) 1165–1184.

- [20] A. Taherizadeh, D. E. Green, J. W. Yoon, Evaluation of advanced anisotropic models with mixed hardening for general associated and non-associated flow metal plasticity, *International Journal of Plasticity* 27 (11) (2011) 1781–1802.
- [21] T. Kuwabara, K. Hashimoto, E. Iizuka, J. W. Yoon, Effect of anisotropic yield functions on the accuracy of hole expansion simulations, *Journal of Materials Processing Technology* 211 (3) (2011) 475–481.
- [22] A. Phillips, C. Liu, J. Justusson, An experimental investigation of yield surfaces at elevated temperatures, *Acta Mechanica* 14 (2-3) (1972) 119–146.
- [23] A. Phillips, Yield surfaces of pure aluminum at elevated temperatures, in: *Thermoinelasticity*, Springer, 1970, pp. 241–258.
- [24] A. Phillips, T. Juh-Ling, The effect of loading path on the yield surface at elevated temperatures, *International Journal of Solids and Structures* 8 (4) (1972) 463–474.
- [25] M. Stout, P. Martin, D. Helling, G. Canova, Multiaxial yield behavior of 1100 aluminum following various magnitudes of prestrain, *International Journal of Plasticity* 1 (2) (1985) 163–174.
- [26] A. A. Brown, An experimental study of the strain-space formulation of plasticity, University of California, Berkeley, 2000.
- [27] K. Wegener, M. Schlegel, Suitability of yield functions for the approximation of subsequent yield surfaces, *International Journal of Plasticity* 12 (9) (1996) 1151–1177.
- [28] J. Hahm, K. Kim, Anisotropic work hardening of steel sheets under plane stress, *International Journal of Plasticity* 24 (7) (2008) 1097–1127.
- [29] A. S. Khan, A. Pandey, T. Stoughton, Evolution of subsequent yield surfaces and elastic constants with finite plastic deformation. part ii: A very high work hardening aluminum alloy (annealed 1100 al), *International Journal of Plasticity* 26 (10) (2010) 1421 – 1431.

- [30] P. Armstrong, J. Hockett, O. Sherby, Large strain multidirectional deformation of 1100 aluminum at 300 k, *Journal of the Mechanics and Physics of Solids* 30 (1-2) (1982) 37–58.
- [31] M. P. Miller, Improved constitutive laws for finite strain inelastic deformation, Ph.D. thesis, Georgia Institute of Technology (1993).
- [32] T. Kuwabara, A. Van Bael, E. Iizuka, Measurement and analysis of yield locus and work hardening characteristics of steel sheets with different r-values, *Acta Materialia* 50 (14) (2002) 3717–3729.
- [33] A. Lopes, F. Barlat, J. Gracio, J. F. Duarte, E. Rauch, Effect of texture and microstructure on strain hardening anisotropy for aluminum deformed in uniaxial tension and simple shear, *International Journal of Plasticity* 19 (1) (2003) 1–22.
- [34] N. Abedrabbo, F. Pourboghra, J. Carsley, Forming of aluminum alloys at elevated temperatures—part 1: Material characterization, *International Journal of plasticity* 22 (2) (2006) 314–341.
- [35] N. Abedrabbo, F. Pourboghra, J. Carsley, Forming of aluminum alloys at elevated temperatures—part 2: Numerical modeling and experimental verification, *International Journal of Plasticity* 22 (2) (2006) 342–373.
- [36] N. Abedrabbo, F. Pourboghra, J. Carsley, Forming of aa5182-o and aa5754-o at elevated temperatures using coupled thermo-mechanical finite element models, *International Journal of Plasticity* 23 (5) (2007) 841–875.
- [37] H. Aretz, A simple isotropic-distortional hardening model and its application in elastic–plastic analysis of localized necking in orthotropic sheet metals, *International Journal of Plasticity* 24 (9) (2008) 1457–1480.
- [38] T. B. Stoughton, J. W. Yoon, Anisotropic hardening and non-associated flow in proportional loading of sheet metals, *International Journal of Plasticity* 25 (9) (2009) 1777–1817.

- [39] H. Li, X. Hu, H. Yang, L. Li, Anisotropic and asymmetrical yielding and its distorted evolution: Modeling and applications, *International Journal of Plasticity* 82 (2016) 127 – 158. doi:<https://doi.org/10.1016/j.ijplas.2016.03.002>.  
URL <http://www.sciencedirect.com/science/article/pii/S0749641916300262>
- [40] J. W. Yoon, Y. Lou, J. Yoon, M. V. Glazoff, Asymmetric yield function based on the stress invariants for pressure sensitive metals, *International Journal of Plasticity* 56 (2014) 184 – 202. doi:<https://doi.org/10.1016/j.ijplas.2013.11.008>.  
URL <http://www.sciencedirect.com/science/article/pii/S0749641913002131>
- [41] E.-H. Lee, T. B. Stoughton, J. W. Yoon, A yield criterion through coupling of quadratic and non-quadratic functions for anisotropic hardening with non-associated flow rule, *International Journal of Plasticity* 99 (2017) 120 – 143.
- [42] B. Lester, W. Scherzinger, An evolving effective stress approach to anisotropic distortional hardening, *International Journal of Solids and Structures* 143 (2018) 194 – 208.
- [43] E.-H. Lee, T. B. Stoughton, J. W. Yoon, Kinematic hardening model considering directional hardening response, *International Journal of Plasticity* 110 (2018) 145 – 165.
- [44] Y. Lou, J. W. Yoon, Anisotropic yield function based on stress invariants for bcc and fcc metals and its extension to ductile fracture criterion, *International Journal of Plasticity* 101 (2018) 125 – 155.
- [45] F. Kabirian, A. S. Khan, Anisotropic yield criteria in stress space for materials with yield asymmetry, *International Journal of Solids and Structures* 67-68 (2015) 116 – 126. doi:<https://doi.org/10.1016/j.ijsolstr.2015.04.006>.

URL <http://www.sciencedirect.com/science/article/pii/S002076831500147X>

- [46] R. Cardoso, O. Adetoro, A generalisation of the hill's quadratic yield function for planar plastic anisotropy to consider loading direction, *International Journal of Mechanical Sciences* 128-129 (2017) 253 – 268.
- [47] Crystal plasticity finite element analysis of ferritic stainless steel for sheet formability prediction, *International Journal of Plasticity* 93 (2017) 26 – 45, special Issue on Constitutive Descriptions of Plasticity at Various Scales in memory of Prof. Jos J. Grcio.
- [48] Multi-level modelling of mechanical anisotropy of commercial pure aluminium plate: Crystal plasticity models, advanced yield functions and parameter identification, *International Journal of Plasticity* 66 (2015) 3 – 30, plasticity of Textured Polycrystals In Honor of Prof. Paul Van Houtte.
- [49] R. Krieg, S. Key, Accurate representation of large strain non-proportional plastic flow in ductile materials, Tech. rep., Sandia National Labs., Albuquerque, NM (USA); RE/SPEC, Inc., Albuquerque, NM (USA) (1984).
- [50] J. Schmitt, E. Aernoudt, B. Baudelet, Yield loci for polycrystalline metals without texture, *Materials Science and Engineering* 75 (1) (1985) 13–20.
- [51] C. Teodosiu, Z. Hu, Evolution of the intragranular microstructure at moderate and large strains: modelling and computational significance, *Simulation of materials processing: theory, methods and application*. Rotterdam: Balkema (1995) 173–82.
- [52] C. Teodosiu, Z. Hu, Microstructure in the continuum modelling of plastic anisotropy, in: *Nineteenth Riso International Symposium on Materials Science 1998*, 1998, pp. 149–168.
- [53] H. Haddadi, S. Bouvier, M. Banu, C. Maier, C. Teodosiu, Towards an accurate description of the anisotropic behaviour of sheet metals under large plastic defor-

- mations: modelling, numerical analysis and identification, *International Journal of Plasticity* 22 (12) (2006) 2226–2271.
- [54] M. Van Riel, A. van den Boogaard, Stress–strain responses for continuous orthogonal strain path changes with increasing sharpness, *Scripta materialia* 57 (5) (2007) 381–384.
- [55] H. Wang, Y. Yan, M. Wan, X. Wu, Experimental investigation and constitutive modeling for the hardening behavior of 5754o aluminum alloy sheet under two-stage loading, *International Journal of Solids and Structures* 49 (26) (2012) 3693–3710.
- [56] S. Boers, P. Schreurs, M. Geers, V. Levkovitch, J. Wang, B. Svendsen, Experimental characterization and model identification of directional hardening effects in metals for complex strain path changes, *International Journal of Solids and Structures* 47 (10) (2010) 1361–1374.
- [57] M. Oliveira, J. Alves, B. Chaparro, L. Menezes, Study on the influence of work-hardening modeling in springback prediction, *International Journal of Plasticity* 23 (3) (2007) 516–543.
- [58] S. Bouvier, B. Gardey, H. Haddadi, C. Teodosiu, Characterization of the strain-induced plastic anisotropy of rolled sheets by using sequences of simple shear and uniaxial tensile tests, *Journal of materials processing technology* 174 (1) (2006) 115–126.
- [59] S. Bouvier, J. Alves, M. Oliveira, L. Menezes, Modelling of anisotropic work-hardening behaviour of metallic materials subjected to strain-path changes, *Computational Materials Science* 32 (3) (2005) 301–315.
- [60] D. Bammann, E. Aifantis, A model for finite-deformation plasticity, *Acta Mechanica* 69 (1-4) (1987) 97–117.
- [61] R. J. Asaro, T. C. Lowe, Crystal plasticity analysis of large-strain shear, Sandia National Laboratory Report SAND85-8245.

- [62] M. Miller, E. Harley, D. Bammann, Reverse yield experiments and internal variable evolution in polycrystalline metals, *International Journal of Plasticity* 15 (1) (1999) 93–117.
- [63] M. François, A plasticity model with yield surface distortion for non proportional loading, *International Journal of Plasticity* 17 (5) (2001) 703–717.
- [64] A. Shutov, J. Ihlemann, A viscoplasticity model with an enhanced control of the yield surface distortion, *International Journal of Plasticity* 39 (2012) 152–167.
- [65] D. Bammann, M. Chiesa, G. Johnson, Modeling large deformation and failure in manufacturing processes, *Theoretical and Applied Mechanics* (9) (1996) 359–376.
- [66] J. Chaboche, A review of some plasticity and viscoplasticity constitutive theories, *International Journal of Plasticity* 24 (10) (2008) 1642–1693.
- [67] F. Barlat, J. J. Gracio, M.-G. Lee, E. F. Rauch, G. Vincze, An alternative to kinematic hardening in classical plasticity, *International Journal of Plasticity* 27 (9) (2011) 1309–1327.
- [68] J. Ha, J.-H. Kim, F. Barlat, M.-G. Lee, Continuous strain path change simulations for sheet metal, *Computational Materials Science* 82 (2014) 286–292.
- [69] W. He, S. Zhang, H. Song, An extended homogenous yield function based anisotropic hardening model for description of anisotropic hardening behavior of materials, *International Journal of Mechanical Sciences* 77 (2013) 343–355.
- [70] G. Vincze, F. Barlat, E. F. Rauch, C. N. Tomé, M. C. Butuc, J. J. Grácio, Experiments and modeling of low carbon steel sheet subjected to double strain path changes, *Metallurgical and Materials Transactions A* 44 (10) (2013) 4475–4479.
- [71] R. Regueiro, D. Bammann, E. Marin, K. Garikipati, A nonlocal phenomenological anisotropic finite deformation plasticity model accounting for dislocation defects, *Journal of Engineering Materials and Technology* 124 (3) (2002) 380–387.

- [72] V. C. Prantil, J. T. Jenkins, P. R. Dawson, An analysis of texture and plastic spin for planar polycrystals, *Journal of the Mechanics and Physics of Solids* 41 (8) (1993) 1357–1382.
- [73] V. C. Prantil, An analytical description of macroscopic anisotropy for planar polycrystalline aggregates, Cornell University, January, 1992.
- [74] E. Onat, F. Leckie, Representation of mechanical behavior in the presence of changing internal structure, *Journal of Applied Mechanics* 55 (1) (1988) 1–10.
- [75] S. G. Advani, C. L. Tucker III, The use of tensors to describe and predict fiber orientation in short fiber composites, *Journal of Rheology* 31 (8) (1987) 751–784.
- [76] S. G. Advani, C. L. Tucker III, Closure approximations for three-dimensional structure tensors, *Journal of Rheology* 34 (3) (1990) 367–386.
- [77] V. Lubarda, D. Krajcinovic, Some fundamental issues in rate theory of damage-elastoplasticity, *International Journal of Plasticity* 11 (7) (1995) 763–797.
- [78] M. Kachanov, Continuum model of medium with cracks, *Journal of the engineering mechanics division* 106 (5) (1980) 1039–1051.
- [79] K. Ken-Ichi, Distribution of directional data and fabric tensors, *International Journal of Engineering Science* 22 (2) (1984) 149–164.
- [80] M. Satake, Fabric tensor in granular materials.
- [81] P. Zysset, A. Curnier, An alternative model for anisotropic elasticity based on fabric tensors, *Mechanics of Materials* 21 (4) (1995) 243–250.
- [82] P. Zysset, A. Curnier, A 3d damage model for trabecular bone based on fabric tensors, *Journal of biomechanics* 29 (12) (1996) 1549–1558.
- [83] M. Rashid, Texture evolution and plastic response of two-dimensional polycrystals, *Journal of the Mechanics and Physics of Solids* 40 (5) (1992) 1009–1029.

- [84] J. Ning, E. Aifantis, Anisotropic yield and plastic flow of polycrystalline solids, *International journal of plasticity* 12 (10) (1996) 1221–1240.
- [85] H. W. Cho, Y. F. Dafalias, Distortional and orientational hardening at large viscoplastic deformations, *International Journal of Plasticity* 12 (7) (1996) 903–925.
- [86] E. Marin, D. Bammann, R. Regueiro, G. Johnson, On the formulation, parameter identification and numerical integration of the emmi model: Plasticity and isotropic damage, Sandia National Laboratories, Livermore, CA, Report No. SAND2006-0200.
- [87] E. Lee, D. Liu, Finite-strain elastic-plastic theory with application to plane-wave analysis, *Journal of Applied Physics* 38 (1) (1967) 19–27.
- [88] E. H. Lee, *Elastic-plastic deformation at finite strains*, ASME, 1969.
- [89] B. D. Coleman, W. Noll, The thermodynamics of elastic materials with heat conduction and viscosity, *Archive for Rational Mechanics and Analysis* 13 (1) (1963) 167–178.
- [90] B. D. Coleman, M. E. Gurtin, Thermodynamics with internal state variables, *The Journal of Chemical Physics* 47 (2) (1967) 597–613.
- [91] U. Kocks, H. Mecking, A mechanism for static and dynamic recovery, *Strength of Metals and Alloys* (1980) 345–350.
- [92] Y. Estrin, H. Mecking, A unified phenomenological description of work hardening and creep based on one-parameter models, *Acta Metallurgica* 32 (1) (1984) 57–70.
- [93] E. Nes, Recovery revisited, *Acta metallurgica et materialia* 43 (6) (1995) 2189–2207.
- [94] R. Regueiro, D. Bammann, E. Marin, K. Garikipati, A nonlocal phenomenological anisotropic finite deformation plasticity model accounting for dislocation

- defects, *Transactions of the ASME: Journal of engineering materials and technology* 124 (3) (2002) 380–386.
- [95] Y. Dafalias, A missing link in the formulation and numerical implementation of finite transformation elastoplasticity, *Constitutive equations: Macro and computational aspects* (1984) 25–40.
- [96] B. Loret, On the effects of plastic rotation in the finite deformation of anisotropic elastoplastic materials, *Mechanics of Materials* 2 (4) (1983) 287–304.
- [97] A. Adetokunbo, Enhancing Verification and Validation in Plasticity Using Material Point Simulators, Github:<https://github.com/tokshgithub/Multidimensional-Material-Point-Simulator-for-BCJ-and-EMMI.git>, 2009.
- [98] A. A. Adedoyin, A continuum mechanics approach to modeling and simulating engineering materials undergoing phase transformation using the evolving micro-structural model of inelasticity, Mississippi State University, 2014.
- [99] J. E. Hockett, On relating the flow stress of aluminum to strain, strain rate, and temperature., Tech. rep., Los Alamos Scientific Lab., N. Mex. (1966).
- [100] Hibbett, Karlsson, Sorensen, *ABAQUS/standard: User's Manual, Vol. 1*, Hibbitt, Karlsson & Sorensen, 1998.
- [101] D. J. Bammann, Modeling temperature and strain rate dependent large deformations of metals, *Appl. Mech. Rev* 43 (5) (1990) S312–S319.
- [102] P. Dawson, P. Follansbee, The variable threshold rod experiment: a comparison of measured and computed deformations, *Journal of engineering materials and technology* 115 (2) (1993) 211–219.
- [103] J. Hockett, O. Sherby, Large strain deformation of polycrystalline metals at low homologous temperatures, *Journal of the Mechanics and Physics of Solids* 23 (2) (1975) 87–98.

- [104] P. Follansbee, U. Kocks, A constitutive description of the deformation of copper based on the use of the mechanical threshold stress as an internal state variable, *Acta Metallurgica* 36 (1) (1988) 81–93.
- [105] B. C. Templin, Towards modeling the anisotropic behavior of polycrystalline materials due to texture using a second order structure tensor, Ph.D. thesis, Mississippi State University (2014).
- [106] K. Ken-Ichi, Distribution of directional data and fabric tensors, *International Journal of Engineering Science* 22 (2) (1984) 149–164.

## Appendix A. Incorporating anisotropy plasticity due to texture: generalities

The goal here is to derive and incorporate the anisotropic plasticity due to texture in the EMMI model. Two important parameters for the plasticity model are derived in this appendix: the plastic rate of deformation  $\mathbf{d}_p$  and the plastic spin  $\mathbf{w}^p$ .

It is assumed that the orientation of grains in aggregates are represented by a continuous function representing the crystal orientation as orientation distribution functions (ODF). In general the estimation of the distribution is first determined by achieving a model or parametric form function that describes the orientation distribution. Assuming that  $\Gamma(\omega)$  is the given distribution density depending upon the unit vector  $\omega$ . We want to approximate the distribution density by  $F(\omega)$  which involves indetermined parameters. In this study, ODF functions are represented by an infinite series in polynomial form shown below:

$$F(\omega) = a + a_i\omega_i + a_{ij}\omega_i\omega_j + a_{ijkl}\omega_i\omega_j\omega_k\omega_l + \dots \quad (\text{A.1})$$

We also need a criterion to estimate the ODF parameters. The typical approximation is to minimize the least square approximation as

$$\int [F(\omega) - \Gamma(\omega)]^2 d\omega \longrightarrow Min \quad (\text{A.2})$$

The ODF satisfies the conservative equation thanks to the fact that the number of crystals in any initial interval of orientation does not change. Taking inspiration from the previous work by Advani and Tucker [75, 76], we assume that the ODF has the periodicity property which indicates that

$$F(\omega) = F(-\omega). \quad (\text{A.3})$$

Eq.(A.3) can be normalized by

$$\oint dS = \int_0^{2\pi} \int_0^\pi \sin(\theta) d\theta d\phi = 4\pi, \quad \oint F(\omega) d\omega = 1. \quad (\text{A.4})$$

Prantil [72] showed that the ODF satisfies the continuity equation

$$\dot{F}(\omega) + F(\omega)\nabla \cdot \dot{\omega} = 0. \quad (\text{A.5})$$

The parameters in Eq.(A.1) known as fabric tensor of third kind proposed by Kanatani [106] can be derived from the equation

$$a_{i_1, i_2, i_3, \dots, i_n} = \oint \Gamma(\omega) \left\{ \omega_{i_1} \omega_{i_2} \omega_{i_3} \cdots \omega_{i_n} \right\} d\omega, \quad (\text{A.6})$$

where  $\left\{ \omega_{i_1} \omega_{i_2} \omega_{i_3} \cdots \omega_{i_n} \right\}$  is the deviatoric part of  $\omega_{i_1} \omega_{i_2} \omega_{i_3} \cdots \omega_{i_n}$  tensor. Using the first two terms and by truncating the higher order terms, the ODF yields the expression

$$F(\omega) = \frac{1}{2\pi} + \frac{2}{\pi} a_{ij} f_{ij}(\omega) \quad (\text{A.7})$$

where

$$f_{ij}(\omega) = \omega_i \omega_j - \frac{1}{3} \delta_{ij} \quad (\text{A.8})$$

$$a_{ij} = \oint \Gamma(\omega) f_{ij}(\omega) d\omega.$$

In Eq.(A.8)  $a_{ij}$  is the structure tensor component. Therefore, the orientation of actual experimental data represented by  $\Gamma(\omega)$  helps to identify a second rank tensor. Then, the statistical distribution of the orientation can be represented by Eq.(A.7).

While the stress varies during the deformation process in materials, the crystal structure may orient in different directions. The reorientation of the crystal indicates that the tensorial constant  $a_{ij}$  in the ODF should vary in order to carry out the information of the orientation of the crystal in aggregate. For this we intend to formulate an evolution equation for the structure tensor to be able to carry the anisotropic texture information during deformation process.

The continuity equation Eq.(A.5) indicates that the grain orientation update  $\dot{\omega}$  should be determined. The plastic spin  $\mathbf{w}_p$  is the main cause of the grain reorientation. Then, from Prantil [72] the grain orientation update equation can be written as

$$\dot{\omega} = \mathbf{w}_p \omega \quad (\text{A.9})$$

It follows that, the Jaumann derivative of the grain orientation is given by

$$\tilde{\omega} = \dot{\omega} - \mathbf{w} \omega = \lambda_g \mathbf{d}_p \omega - \lambda_g (\omega \cdot \mathbf{d}_p \omega) \omega \quad (\text{A.10})$$

Substituting the above Eq.( A.10) into the continuity equation Eq.(A.5) gives

$$\nabla \cdot \tilde{\omega} = \nabla \cdot (\lambda_g \mathbf{d}_p \omega - \lambda_g (\omega \cdot \mathbf{d}_p \omega) \omega) = -2\lambda_g (\omega \cdot \mathbf{d}_p \omega) \quad (\text{A.11})$$

with

$$\dot{F}(\omega) = F(\omega) (2\lambda_g \omega \cdot \mathbf{d}_p \omega). \quad (\text{A.12})$$

The material time derivative of the structure tensor definition is

$$\dot{a}_{ij} = \overline{\dot{F}(\omega) f_{ij}(\omega)} = \oint \dot{F}(\omega) f_{ij}(\omega) d\omega + \oint F(\omega) \dot{f}_{ij}(\omega) d\omega. \quad (\text{A.13})$$

From the grain orientation update equation Eq.(A.11) we get

$$\begin{aligned} \dot{f}_{ij} &= \dot{\omega} \otimes \omega + \omega \otimes \dot{\omega} \\ &= \lambda_g ((\omega \otimes \omega - \mathbf{I}) \mathbf{d}_p \omega) \otimes \omega + \lambda_g \omega ((\omega \otimes \omega - \mathbf{I}) \mathbf{d}_p \omega) \\ &= \lambda_g (\mathbf{d}_p \omega \otimes \omega + \omega \otimes \mathbf{d}_p \omega - 2(\omega \cdot \mathbf{d}_p \omega) (\omega \otimes \omega)) \end{aligned} \quad (\text{A.14})$$

and the equation Eq.(A.15) expands as follows:

$$\begin{aligned} \dot{a}_{ij} &= \overline{\dot{F}(\omega) f_{ij}(\omega)} = \oint \dot{F}(\omega) f_{ij}(\omega) d\omega + \oint F(\omega) \dot{f}_{ij}(\omega) d\omega \\ &= \oint F(\omega) (2\lambda_g (\omega \cdot \mathbf{d}_p \omega)) f_{ij}(\omega) d\omega \\ &\quad + \oint \dot{F}(\omega) \lambda_g (\mathbf{d}_p \omega \otimes \omega + \omega \otimes \mathbf{d}_p \omega - 2(\omega \cdot \mathbf{d}_p \omega) (\omega \otimes \omega)) d\omega \\ &= 2\lambda_g (\omega \cdot \mathbf{d}_p \omega) \oint F(\omega) f_{ij}(\omega) d\omega \\ &\quad + \lambda_g \oint F(\omega) (\mathbf{d}_p \omega \otimes \omega + \omega \otimes \mathbf{d}_p \omega - 2(\omega \cdot \mathbf{d}_p \omega) (\omega \otimes \omega)) d\omega \\ &= 2\lambda_g (\omega \cdot \mathbf{d}_p \omega) a_{ij} + \lambda_g \oint F(\omega) (\mathbf{d}_p \omega \otimes \omega + \omega \otimes \mathbf{d}_p \omega) d\omega \\ &\quad - 2\lambda_g (\omega \cdot \mathbf{d}_p \omega) \oint F(\omega) \left( \omega \otimes \omega - \frac{1}{3} \delta_{ij} + \frac{1}{3} \delta_{ij} \right) d\omega \\ &= -2\lambda_g (\omega \cdot \mathbf{d}_p \omega) a_{ij} + \lambda_g \left( \mathbf{a} \mathbf{d}_p + \mathbf{d}_p \mathbf{a} + \frac{2}{3} \mathbf{d}_p \right) \\ &\quad + \frac{2}{3} \lambda_g (\omega \cdot \mathbf{d}_p \omega) \oint F(\omega) \delta_{ij} d\omega \end{aligned} \quad (\text{A.15})$$

with

$$\dot{\mathbf{a}} = \lambda_g \left( \mathbf{a} \mathbf{d}_p + \mathbf{d}_p \mathbf{a} + \frac{2}{3} \mathbf{d}_p \right) - 2\lambda_g \mathbf{B} : \mathbf{d}_p + \frac{2}{3} \lambda_g (\omega \cdot \mathbf{d}_p \omega) \mathbf{I} \quad (\text{A.16})$$

Based on the multiplicative decomposition of the deformation gradient into elastic and plastic parts  $\mathbf{F} = \mathbf{F}^e \mathbf{F}^p$  the evolution equation for the structure tensor  $\mathbf{a}$  in the intermediate configuration is

$$\tilde{\mathbf{a}} = \mathbf{F}^p \left( \overline{\mathbf{F}^{p^{-1}} \mathbf{a} \mathbf{F}^p} \right) \mathbf{F}^{p^{-1}} = \dot{\mathbf{a}} - \mathbf{l}_p \mathbf{a} + \mathbf{a} \mathbf{l}_p. \quad (\text{A.17})$$

Combining Eqs.(A.15) and (A.17) the evolution equation for the structure tensor  $\mathbf{a}$  becomes

$$\begin{aligned} \tilde{\mathbf{a}} &= \dot{\mathbf{a}} - \mathbf{w}_p \mathbf{a} + \mathbf{a} \mathbf{w}_p \\ &= \mathbf{a} \mathbf{w}_p - \mathbf{w}_p \mathbf{a} + \lambda_g \left( \mathbf{a} \mathbf{d}_p + \mathbf{d}_p \mathbf{a} + \frac{2}{3} \mathbf{d}_p \right) \\ &\quad + \frac{2}{3} \lambda_g (\boldsymbol{\omega} \cdot \mathbf{d}_p \boldsymbol{\omega}) \mathbf{I} - 2 \lambda_g \mathbf{B} : \mathbf{d}_p \end{aligned} \quad (\text{A.18})$$

where  $\mathbf{B}$  is a fourth rank tensor defined as

$$B_{ijkl} = \oint F(\boldsymbol{\omega}) \omega_i \omega_j \omega_k \omega_l d\boldsymbol{\omega}. \quad (\text{A.19})$$

## Appendix B. Closure approximation

The structure tensor  $a_{ij}$  is the moment of the distribution function  $F(\boldsymbol{\omega})$ , and its evolution equation of  $\mathbf{a}$  represents a closure problem. The evolution equation Eq.(A.18) for any tensor always contains the next higher even-order tensor (Advani and Tucker [75, 76]). Therefore, the evolution equation of second order structure tensor contains a fourth order tensor  $B_{ijkl}$ . It is required to develop some approximation to obtain a close set of evolution equations. The closure approximation should contain several assumptions including

1. the approximation must only be from the lower order orientation tensors and the unit tensor;
2. the approximation must satisfy normalization conditions in the equations as below

$$a_{ii} = 1, B_{ijkk} = a_{ij}; \quad (\text{B.1})$$

3. the approximation should maintain the symmetry of orientation tensor:

$$\left\{ \begin{array}{l} a_{ij} = a_{ji} \\ B_{ijkl} = B_{jikl} = B_{kijl} = B_{lijk} = B_{klji}. \end{array} \right. \quad (\text{B.2})$$

In the subsequent we use a linear closure approximation for the fourth order tensor  $B_{ijkl}$  using all of the products of  $a_{ij}$  and  $\delta_{ij}$ .

For three-dimensional orientation the linear approximation of fourth order tensor becomes

$$\begin{aligned} \hat{B}_{ijkl} = & \frac{1}{7} (a_{ij}\delta_{kl} + a_{ik}\delta_{jl} + a_{il}\delta_{jk} + a_{kl}\delta_{ij} + a_{jl}\delta_{ik} + a_{jk}\delta_{il}) \\ & - \frac{1}{35} (\delta_{ij}\delta_{kl} + \delta_{ik}\delta_{jl} + \delta_{il}\delta_{jk}) \end{aligned} \quad (\text{B.3})$$

Another way to form a closure approximation is to omit the linear terms and take the product of lower order tensors. This is known as quadratic closure,  $\tilde{B}_{ijkl}$ , which is defined as

$$\tilde{B}_{ijkl} = a_{ij}a_{kl} \quad (\text{B.4})$$

The quadratic closure does not have all the symmetry properties of the components  $B_{ijkl}$  but it has the symmetry properties of elasticity tensor and presents no difficulty for mechanical property predictions. It is worth mentioning that once this approximation is used in the evolution equation, it preserves the symmetry of the tensor  $a_{ij}$ . In dilute short fiber composites, it is shown that the linear closure approximations are exact for a completely random distribution of fiber orientation while the quadratic closure approximations are exact for perfect uniaxial alignments of the fibers. Hence, the combination of the two closure approximations can offer the orientation information for the entire range of orientations.

A hybrid closure approximation  $\bar{B}_{ijkl}$  is constructed by combining the two presented approximations as

$$\bar{B}_{ijkl} = (1 - f) \hat{B}_{ijkl} + \tilde{B}_{ijkl} \quad (\text{B.5})$$

where  $f$  is a generalization of Herman's orientation factor; it is equal to zero for randomly oriented inclusions and unity for perfectly aligned inclusions. The scalar measure  $f$  is defined as

$$f = C_1 a_{ij} a_{ji} - C_2 = \frac{3}{2} a_{ij} a_{ji} - \frac{1}{2} \quad (\text{B.6})$$

for three dimensional orientation which is an invariant of the structure tensor  $\mathbf{a}$ . Applying the closure approximation to the last term in Eq.(A.18) we get

$$b_{ijkl}d_{p,kl} = (1-f) \left( -\frac{1}{35} (2\mathbf{d}_p) + \frac{1}{7} (\mathbf{a}\mathbf{d}_p + \mathbf{d}_p\mathbf{a} + (\mathbf{a} : \mathbf{d}_p) \delta_{ij} + \mathbf{a}\mathbf{d}_p + \mathbf{d}_p\mathbf{a}) \right) \\ + f (\mathbf{a} : \mathbf{d}_p) a_{ij}$$

or in a compact form:

$$\mathbf{B} : \mathbf{d}_p = (1-f) \left( -\frac{1}{35} (2\mathbf{d}_p) + \frac{1}{7} (2\mathbf{a}\mathbf{d}_p + (\mathbf{a} : \mathbf{d}_p) \mathbf{I} + 2\mathbf{d}_p\mathbf{a}) \right) \\ + f (\mathbf{a} : \mathbf{d}_p) \mathbf{a} \quad (\text{B.7})$$

Hence, the final evolution equation of the structure tensor reads:

$$\tilde{\mathbf{a}} = \dot{\mathbf{a}} - \mathbf{w}_p\mathbf{a} + \mathbf{a}\mathbf{w}_p \\ = -2\lambda_g (1-f) \left( -\frac{1}{35} (2\mathbf{d}_p) + \frac{1}{7} (2\mathbf{a}\mathbf{d}_p + (\mathbf{a} : \mathbf{d}_p) \delta_{ij} + 2\mathbf{a}\mathbf{d}_p) \right) \\ - 2\lambda_g f (\mathbf{a} : \mathbf{d}_p) \mathbf{a} + \lambda_g \left( \mathbf{a}\mathbf{d}_p + \mathbf{d}_p\mathbf{a} + \frac{2}{3}\mathbf{d}_p \right) + \frac{2}{3}\lambda_g (\mathbf{a} : \mathbf{d}_p) \mathbf{I} - \mathbf{w}_p\mathbf{a} + \mathbf{a}\mathbf{w}_p \quad (\text{B.8})$$

with the equation

$$(\mathbf{a} : \mathbf{d}_p) = \omega \cdot \mathbf{d}_p \omega \quad (\text{B.9})$$

where  $\lambda_g$  is a geometric parameter dependent on slip system orientation. The plastic spin of the aggregate in the intermediate configuration is defined by averaging the plastic spin in each grain using ODF as

$$\mathbf{w}_p = \oint \mathbf{a}(\omega) \mathbf{w}_g^p(\omega) d\omega = \lambda_g (\mathbf{a}\mathbf{d}_p - \mathbf{d}_p\mathbf{a}).$$

The asymmetric part of the velocity gradient should be added to the skew-symmetric part to obtain the velocity gradient in the deformation process

$$\mathbf{l}_p = \mathbf{d}_p + \mathbf{w}_p \quad (\text{B.10})$$

The symmetric part of velocity gradient  $\mathbf{d}_p$  is defined separately by its magnitude  $\|\mathbf{d}_p\|$  and its direction  $\mathbf{N}$ :

$$\mathbf{d}_p = \|\mathbf{d}_p\| \mathbf{N} \quad (\text{B.11})$$

The magnitude of the symmetric part of the velocity gradient which is called the evolution of plastic flow is written in the unified creep plasticity form as

$$\|\mathbf{d}_p\| = \sqrt{\frac{2}{3}} f(\theta) (\sinh(\Phi))^{n(\theta)} \quad (\text{B.12})$$

where the function  $f(\theta)$  determines the strain rate at which the model transitions from rate-independent to rate-dependent behavior,  $n(\theta)$  is the temperature dependent rate sensitivity parameter and, the term inside the hyperbolic sine function called the plastic potential  $\Phi$  function is defined by the relation

$$\Phi = \left[ \frac{\sigma_{eq}}{\bar{\chi}\bar{\kappa} + Y_0} - 1 \right] \quad (\text{B.13})$$

where  $\sigma_{eq}$  the magnitude of a second rank tensor including the deviatoric part of the Piola-Kirchhoff stress; the back stress is defined as

$$\sigma_{eq} = \sqrt{\frac{2}{3}} \|\boldsymbol{\xi}\| \quad (\text{B.14})$$

with

$$\boldsymbol{\xi} = \boldsymbol{\sigma}' - \frac{2}{3}\boldsymbol{\alpha}. \quad (\text{B.15})$$

Two terms in the denominator of Eq.(B.13) are  $\bar{\kappa}$  and  $\bar{\chi}$  which are related to the dislocation density and the directional distortion.

The directional distortion is defined based on the cosine series as

$$\bar{\chi} = 1 + a_1 \cos(\bar{\eta}) + a_2 \cos 2(\bar{\eta}) + a_3 \cos 3(\bar{\eta}) + a_4 \cos 4(\bar{\eta}). \quad (\text{B.16})$$

The angles in the cosine series are calculated from the angle between the stress tensor  $\boldsymbol{\xi}$  and the structure tensor  $\mathbf{a}$ :

$$\cos(\bar{\eta}) = \cos(\bar{\eta}) = \frac{\boldsymbol{\xi} : \mathbf{a}}{\|\boldsymbol{\xi}\| \|\mathbf{a}\|} \quad (\text{B.17})$$

Since there is no flow surface defined for this model, the plastic potential function  $\Phi$  is used to define the direction of the plastic flow. The direction of plastic flow  $\mathbf{N}^p$  derived as

$$\mathbf{N} = \text{sym} \left( \frac{\partial \bar{\Phi}}{\partial \boldsymbol{\xi}} \right) / \left\| \text{sym} \left( \frac{\partial \bar{\Phi}}{\partial \boldsymbol{\xi}} \right) \right\| \quad (\text{B.18})$$

with

$$\begin{aligned}\frac{\partial \Phi}{\partial \bar{\xi}} &= \partial \left[ \frac{\sigma_{eq}}{\bar{\chi} \bar{\kappa} + Y_0} - 1 \right] / \partial \bar{\xi} = \left( \frac{\partial \sigma_{eq}}{\partial \bar{\xi}} \bar{\chi} \bar{\kappa} - \bar{\kappa} \frac{\partial \bar{\chi}}{\partial \bar{\xi}} \sigma_{eq} \right) / (\bar{\chi} \bar{\kappa})^2 \\ &= \frac{1}{\bar{\chi} \bar{\kappa}} \left( \frac{\partial \sigma_{eq}}{\partial \bar{\xi}} - \frac{\sigma_{eq}}{\bar{\chi}} \frac{\partial \bar{\chi}}{\partial \bar{\xi}} \right)\end{aligned}\quad (\text{B.19})$$

where  $\bar{\chi}$  and  $\bar{\kappa}$  are scalars which are related toward the equation

$$\begin{aligned}\mathbf{N} &= \text{sym} \left( \frac{\partial \Phi}{\partial \bar{\xi}} \right) / \left\| \text{sym} \left( \frac{\partial \Phi}{\partial \bar{\xi}} \right) \right\| \\ &= \frac{1}{\bar{\chi} \bar{\kappa}} \text{sym} \left( \frac{\partial \sigma_{eq}}{\partial \bar{\xi}} - \frac{\sigma_{eq}}{\bar{\chi}} \frac{\partial \bar{\chi}}{\partial \bar{\xi}} \right) / \left\| \text{sym} \left( \frac{\partial \sigma_{eq}}{\partial \bar{\xi}} - \frac{\sigma_{eq}}{\bar{\chi}} \frac{\partial \bar{\chi}}{\partial \bar{\xi}} \right) \right\|\end{aligned}\quad (\text{B.20})$$

with

$$\frac{\partial \sigma_{eq}}{\partial \bar{\xi}} = \sqrt{\frac{3}{2}} \frac{\boldsymbol{\xi}}{\|\boldsymbol{\xi}\|}$$

and

$$\begin{aligned}\frac{\partial \bar{\chi}}{\partial \bar{\xi}} &= \frac{\partial \bar{\chi}}{\partial \cos(\bar{\eta})} \frac{\partial \cos(\bar{\eta})}{\partial \bar{\xi}} = \frac{\partial \bar{\chi}}{\partial \cos(\bar{\eta})} \partial \left( \frac{\boldsymbol{\xi} : \mathbf{a}}{\|\boldsymbol{\xi}\| \|\mathbf{a}\|} \right) / \partial \bar{\xi} \\ &= \frac{\partial \bar{\chi}}{\partial \cos(\bar{\eta})} \left( \frac{\partial (\boldsymbol{\xi} : \mathbf{a})}{\partial \bar{\xi}} \|\boldsymbol{\xi}\| \|\mathbf{a}\| - \frac{\partial (\|\boldsymbol{\xi}\| \|\mathbf{a}\|)}{\partial \bar{\xi}} (\boldsymbol{\xi} : \mathbf{a}) \right) / \|\boldsymbol{\xi}\|^2 \|\mathbf{a}\|^2 \\ &= \frac{1}{\|\boldsymbol{\xi}\| \|\mathbf{a}\|} \frac{\partial \bar{\chi}}{\partial \cos(\bar{\eta})} \left[ \frac{\partial (\boldsymbol{\xi} : \mathbf{a})}{\partial \bar{\xi}} - \frac{\partial (\|\boldsymbol{\xi}\| \|\mathbf{a}\|)}{\partial \bar{\xi}} \frac{(\boldsymbol{\xi} : \mathbf{a})}{\|\boldsymbol{\xi}\| \|\mathbf{a}\|} \right] \\ &= \frac{1}{\|\boldsymbol{\xi}\| \|\mathbf{a}\|} \frac{\partial \bar{\chi}}{\partial \cos(\bar{\eta})} \left[ \mathbf{a} - \frac{\partial (\|\boldsymbol{\xi}\| \|\mathbf{a}\|)}{\partial \bar{\xi}} \frac{(\boldsymbol{\xi} : \mathbf{a})}{\|\boldsymbol{\xi}\| \|\mathbf{a}\|} \right] \\ &= \frac{1}{\|\boldsymbol{\xi}\| \|\mathbf{a}\|} \frac{\partial \bar{\chi}}{\partial \cos(\bar{\eta})} \left[ \mathbf{a} - \frac{\boldsymbol{\xi}}{\|\boldsymbol{\xi}\|} \frac{(\boldsymbol{\xi} : \mathbf{a})}{\|\boldsymbol{\xi}\|} \right] \\ &= \frac{1}{\|\boldsymbol{\xi}\| \|\mathbf{a}\|} \frac{\partial \bar{\chi}}{\partial \cos(\bar{\eta})} \left[ \mathbf{a} - \left( \frac{(\boldsymbol{\xi} : \mathbf{a})}{(\boldsymbol{\xi} : \boldsymbol{\xi})} \right) \boldsymbol{\xi} \right] \\ &= \frac{a_1 + 4a_2 \cos(\bar{\eta}) + 3a_3 (4 \cos^2(\bar{\eta}) - 1) + 16a_4 \cos(\bar{\eta}) (4 \cos^2(\bar{\eta}) - 1)}{\|\boldsymbol{\xi}\| \|\mathbf{a}\|} \\ &\quad \times \left[ \mathbf{a} - \left( \frac{(\boldsymbol{\xi} : \mathbf{a})}{(\boldsymbol{\xi} : \boldsymbol{\xi})} \right) \boldsymbol{\xi} \right]\end{aligned}\quad (\text{B.21})$$

where the following relations

$$\frac{\partial \bar{\chi}}{\partial \cos(\bar{\eta})} = a_1 + 4a_2 \cos(\bar{\eta}) + 3a_3 (4 \cos^2(\bar{\eta}) - 1) + 16a_4 \cos(\bar{\eta}) (4 \cos^2(\bar{\eta}) - 1),$$

$$\frac{\partial (\|\boldsymbol{\xi}\| \|\mathbf{a}\|)}{\partial \bar{\xi}} = \frac{\partial (\|\boldsymbol{\xi}\|)}{\partial \bar{\xi}} \|\mathbf{a}\| = \frac{\boldsymbol{\xi}}{\|\boldsymbol{\xi}\|} \|\mathbf{a}\|,$$

$$\|\boldsymbol{\xi}\|^2 = \boldsymbol{\xi} : \boldsymbol{\xi}$$

and

$$\frac{\partial (\boldsymbol{\xi} : \mathbf{a})}{\partial \boldsymbol{\xi}} = \mathbf{a}$$

hold.